



저작자표시-비영리-변경금지 2.0 대한민국

이용자는 아래의 조건을 따르는 경우에 한하여 자유롭게

- 이 저작물을 복제, 배포, 전송, 전시, 공연 및 방송할 수 있습니다.

다음과 같은 조건을 따라야 합니다:



저작자표시. 귀하는 원저작자를 표시하여야 합니다.



비영리. 귀하는 이 저작물을 영리 목적으로 이용할 수 없습니다.



변경금지. 귀하는 이 저작물을 개작, 변형 또는 가공할 수 없습니다.

- 귀하는, 이 저작물의 재이용이나 배포의 경우, 이 저작물에 적용된 이용허락조건을 명확하게 나타내어야 합니다.
- 저작권자로부터 별도의 허가를 받으면 이러한 조건들은 적용되지 않습니다.

저작권법에 따른 이용자의 권리는 위의 내용에 의하여 영향을 받지 않습니다.

이것은 [이용허락규약\(Legal Code\)](#)을 이해하기 쉽게 요약한 것입니다.

[Disclaimer](#)

공학박사학위논문

곤충과 탄성고리의 도약: 소형 개체의
수면 및 유연한 고체 위 도약에 대한
생체모사 역학 연구

Jumping insects and hoops:
Biologically inspired dynamics of
small jumpers on water and
deformable solids

2015 년 8 월

서울대학교 대학원

기계항공공학부

양 은 진

곤충과 탄성고리의 도약: 소형 개체의 수면 및
유연한 고체 위 도약에 대한 생체모사 역학 연구

Jumping insects and hoops: Biologically
inspired dynamics of small jumpers on water
and deformable solids

지도교수 김 호 영

이 논문을 공학박사 학위논문으로 제출함

2015 년 4 월

서울대학교 대학원
기계항공공학부
양 은 진

양은진의 공학박사 학위논문을 인준함
2015 년 6 월

위 원 장	최 해 진	(인)
부 위 원 장	김 호 영	(인)
위 원	조 구 진	(인)
위 원	김 현 정	(인)
위 원	이 상 영	(인)

**Jumping insects and hoops:
Biologically inspired dynamics of
small jumpers on water and
deformable solids**

Eunjin Yang

Department of Mechanical and Aerospace Engineering

Seoul National University

A thesis submitted for the degree of

Doctor of Philosophy

August 2015

Abstract

Jumping insects and hoops: Biologically inspired dynamics of small jumpers on water and deformable solids

Eunjin Yang

Department of Mechanical and Aerospace Engineering
The Graduate School
Seoul National University

Jumping is used by animals as an efficient means of locomotion to escape predators, to catch prey, to increase their speed, or to launch into flight. Small arthropods such as froghoppers, crickets, fleas, grasshoppers, spiders and water striders are able to jump many times their body lengths. Inspired by the superior maneuverability of those insects, biomimetic robots, which mimic the structures, functions and designs of living creatures, are being developed with the goal to jump on land and water. In this study, we combine experimental observation and theoretical analysis to obtain the fundamental understanding of the mechanics of jumping of an artificial jumper and insects on various environment. We started with bio-inspired, simple artificial system jumping on rigid solids, deformable solids, and water, and then move on to the living creatures, grasshoppers and water striders, jumping on leaves and water.

We first consider an elastic hoop as a simple jumper mimicking insects jumping, which can store elastic strain energy in its body structure to propel itself. We investigate the jumping dynamics

of the elastic hoop on various substrates as a model of the jumps of small insects. During a jump the initial elastic strain energy is converted to translational, gravitational, and vibrational energy, and is dissipated by interaction with the substrate and the ambient air. We show that the energy transfer ratio from initial strain energy to translational kinetic energy of hoop depends on the interaction with the substrate which it launches on. When it jumps on rigid solids, the strain energy is initially divided into translational, vibrational, and dissipation energies with a ratio that is constant regardless of the dimension, initial deflection, and the properties of a hoop material. In contrast, when it jumps on deformable substrates such as flexible solids and liquid surface, the energy transfer rate differs depending on the deformation characteristics of the substrates with respect to the hoop properties. This novel result enables us to accurately predict the maximum jump height and efficiency of a hoop with known initial conditions and drag coefficient without resorting to a numerical computation. Our model reduces the optimization of the hoop geometry for maximizing the jump height to a simple algebraic problem.

Next, we focus on the strategy of living creatures jumping on deformable substrates; how grasshoppers control jump on stems with various mass and stiffness, and water striders can jump on water so elegantly. We observe and measure jumps of different species of grasshoppers on artificial stems and water striders on water, and then analyze them mathematically. When they jump, grasshoppers make thrust by virtue of inertial and bending stiffness of stems, whereas water striders exploit capillary force from the water surface which serves the most efficient propulsion on water. We experimentally find an evidence that different species of grasshopper control the power as per the substrate on which they launch. We also find that the

leg stroke speeds of different species of striders correspond to the mathematically calculated optimal values to maximize the takeoff velocity by fully exploiting the capillary force of water. This implies that the jumping striders always tune their leg rotation speed to reach the maximum jumping height that water surface allows. Our mathematical model extracts the essential variables of insect jumping to be useful with further research.

Our work provides a mechanistic understanding how the animal achieves such a dramatic and powerful motion and how artificial jumpers perform on deformable substrates including liquid, as an essential starting point to develop biomimetic semi-aquatic microrobots and robots traveling tough terrain with vegetation. Moreover, this findings raise a question whether such a capability of the insect (optimized behavioral trait and morphology) is a result of evolution or learning, which is hoped to stimulate further research.

Keywords :Jumping, Water surface, Deformable solid, Water strider, Grasshopper, Optimized behavior, Jumping strategy
Student Number : 2008-20759

Contents

Abstract	i
Contents	iv
List of Figures	vii
1 Introduction	1
2 Bio-inspired jumping hoops on various substrates	3
2.1 Introduction	3
2.2 Jumping of an elastic hoop on a rigid solid	4
2.2.1 Experimental methods	5
2.2.2 Jumping height without air drag	7
2.2.3 Jumping height with air drag	10
2.2.4 Optimization of hoop geometry	11
2.3 Jumping of an elastic hoop on flexible solids	17
2.3.1 Experimental methods	18
2.3.2 General features of jumping on basal hoops	18
2.3.3 Takeoff velocity of hoops on basal hoops	21
2.3.4 Efficiency of jumping of hoops on basal hoops	26
2.4 Jumping of an elastic hoop on water	26
2.4.1 Experimental methods	27
2.4.2 Hydrodynamic forces of Jumping on water	30
2.4.3 Takeoff velocity of hoops on water	30
2.4.4 Efficiency of jumping on water	31

CONTENTS

2.5	Conclusions	33
3	Jumping of insects on deformable substrates	36
3.1	Introduction	36
3.2	Jumping of grasshoppers on artificial stems	37
3.2.1	Experimental Methods	37
3.2.2	General features of grasshoppers jumping on artificial stems	37
3.2.3	Model of jumping locomotion of grasshoppers	38
3.2.4	Dynamic analysis of jumping grasshoppers on artificial stems	40
3.2.5	Advantages of grasshoppers locomotion in jumping on stems	42
3.3	Jumping of water striders on water	47
3.3.1	Experimental Methods	47
3.3.2	General features of water striders jumping on water	47
3.3.3	Hydrodynamic forces on the water striders legs	49
3.3.4	Model of locomotion of water striders jump	52
3.3.5	Criteria for exploiting the water surface	54
3.3.6	Dynamic analysis of jumping water striders on water	56
3.3.7	Types of jumping and the regime map	59
3.3.8	Advantages of water striders locomotion in water jumping	63
3.3.9	Relation between water striders morphology and water jumping	66
3.4	Conclusions	67
4	An integrative view of artificial and natural small jumpers on deformable substrates	70
4.1	Equivalent models of water to deformable substrates	70
4.2	An integrative map of efficiency of jumping on deformable substrates	71

CONTENTS

5 Conclusions	73
References	75
Abstract (in Korean)	78

List of Figures

2.1	The jumping sequence of a hoop with radius $R = 16$ mm, width $w = 3$ mm, thickness $c = 125 \mu\text{m}$ and initial deflection $\delta = 14$ mm.	6
2.2	(a) The geometry of an elastic hoop. (b) The experimental apparatus for hoop jumping on flexible solid.	7
2.3	Experimental measurement results for the initial translational kinetic energy $E_{t,0}$ and elastic strain energy E_b , showing a linear relationship between them. The slope of the best fitting line is 0.57.	9
2.4	(Color online) The maximum jumping heights of various hoops with δ ranging up to 12 mm plotted according to the scaling law: $H/h_c \sim c^2\delta^2/R^4$. The straight line corresponds to the jumping height with no air drag obtained by letting $E_{t,0} = 0.57E_b = mgH$. Characteristic error bars are shown in the upper left corner.	10
2.5	Experimentally measured temporal evolution of the height of the hoop with radius $R = 15$ mm, thickness $c = 125 \mu\text{m}$ and initial deflection $\delta = 9$ mm (circles) compared with the theories neglecting (dashed line) and considering (solid line) the air drag. Characteristic error bars are shown in the lower right corner.	12

LIST OF FIGURES

2.6	Dimensionless maximum jumping height versus ϕ . The solid line is from Eq. (2.7) and the broken line is drawn by taking $C_D \rightarrow 0$ in Eq. (2.7). Characteristic error bars are shown in the lower right corner.	12
2.7	The energy conversion ratio from $E_{t,0}$ to E_g (solid line) and to E_d (dashed line).	13
2.8	Maximum jumping heights H_a (in air) versus c/R predicted by Eq. (2.7) that correspond to the conditions of Eqs. (2.8) (solid line), (2.9) (dashed line), and (2.10) (alternate long and short dash line). All the three conditions are met in the hatched area. Filled circles are experimental results. Steel hoops. Inset: Magnified view around the optimum. A: initially the upper segment of a hoop touches the lower one, but the compression force is lower than the maximum allowable actuator force F_m . B: initially the hoop bends until its upper segment touches the lower one, at which state the compression force reaches F_m . C: the hoop is compressed with the maximum allowable actuator force F_m , but the upper segment does not touch the lower one.	15
2.9	Maximum jumping heights H_a (in air) versus c/R predicted by Eq. (2.7) that correspond to the conditions of Eqs. (2.8) (solid line), (2.9) (dashed line), and (2.10) (alternate long and short dash line). All the three conditions are met in the hatched area. Filled circles are experimental results. Polyimide hoops. A: initially the upper segment of a hoop touches the lower one, but the compression force is lower than the maximum allowable actuator force F_m . B: initially the hoop bends until its upper segment touches the lower one, at which state the compression force reaches F_m . C: the hoop is compressed with the maximum allowable actuator force F_m , but the upper segment does not touch the lower one.	16

LIST OF FIGURES

2.10 (a) The geometry of an elastic hoop. (b) The experimental apparatus for hoop jumping on a flexible solid.	19
2.11 The jumping height of hoops on basal hoops. (Blue wedges) a jumping hoop made of steel with radius 15 mm, width 3 mm, thickness 100 μm on a basal hoop made of polyimide with various dimensions; (red circles) a jumping hoop made of steel with radius 20 mm, width 3 mm, thickness 100 μm on a basal hoop made of polyimide with various dimensions.	20
2.12 (a) The sequence of sliced images of hindered jumping mode ($K < 1, \Omega > 2.3$) with displacement prediction (blue and red solid lines). The time gap is 0.3 ms. (b) The velocity of top and bottom of the jumping hoop until take off. The jumping hoop made of polyimide with $R = 20$ mm, $c = 125$ μm , $w = 3$ mm, and $\delta = 5$ mm. The basal hoop made of polyimide with $R = 24$ mm, $c = 125$ μm , and $w = 3$ mm.	21
2.13 (a) The sequence of sliced images of assisted jumping mode ($K > 1, \Omega > 2.3$) with displacement prediction (blue and red solid lines). The time gap is 0.3 ms. (b) The velocity of top and bottom of the jumping hoop until take off. The jumping hoop made of steel with $R = 20$ mm, $c = 100$ μm , $w = 3$ mm, and $\delta = 3$ mm. The basal hoop made of polyimide with $R = 6$ mm, $c = 125$ μm , and $w = 12$ mm.	22
2.14 (a) The sequence of sliced images of ping-ponging mode ($K < 1, \Omega < 2.3$) with displacement prediction (blue and red solid lines). The time gap is 0.3 ms. Red arrow indicates takeoff, and yellow arrows direct bouncing. (b) The velocity of top and bottom of the jumping hoop until the first detachment. The jumping hoop made of steel with $R = 15$ mm, $c = 100$ μm , $w = 3$ mm, and $\delta = 2$ mm. The basal hoop made of polyimide with $R = 10$ mm, $c = 125$ μm , and $w = 3$ mm.	23

LIST OF FIGURES

2.15	The two degree of freedom system of a pair of jumper with double masses model and basal hoops. Subscript 'j' indicates the jumper and 'b' refers to the basal hoop.	24
2.16	The two degree of freedom system of a pair of jumper with a single mass model and basal hoops. Subscript 'j' indicates the jumper and 'b' refers to the basal hoop.	25
2.17	Take off velocity ratio of elastic hoops on basal hoops with respect to the jump on the rigid solid. Circles indicate the natural frequency ration of basal hoop to jumper larger than 2.3, wedges means that smaller than 2.3, red symbols means the stiffness ratio of basal hoop to jumper smaller than 1, and blue symbols indicate the ratio larger than 1.	25
2.18	Jumping efficiency based on the take off velocity ratio of elastic hoops on basal hoops with respect to the jump on the rigid solid. Symbols are the same as Fig. 2.17.	26
2.19	The dependency of the jumping efficiency on natural frequency ratio and stiffness ratio between the basal hoop and the jumper. (Blue lines) double masses jumper model is used for $K < 5$, (black lines)a single mass jumper model is used for $K > 5$	27
2.20	The overlapped images of jumping of a polyimide hoop with radius $R=10$ mm, thickness $c = 125 \mu\text{m}$, and initial deflection $\delta = 7$ mm on water.	28
2.21	(a) The geometry of an elastic hoop. (b) The experimental apparatus for hoop jumping on water.	29
2.22	(a) Coordinates of a hoop jumping off water. (b) Forces on a hoop pushing down the water surface. (c) Coordinates of the wetted circumference element of a hoop.	32

LIST OF FIGURES

2.23	Non-dimensional takeoff velocity of hoops off water. Experimentally measured dimensionless takeoff velocity of hoops with the line indicating the theoretical expectation. Symbols: hoop thickness $75 \mu\text{m}$ (wedges), and $125 \mu\text{m}$ (circles), and hoop radius 10 mm (red), and 15 mm (blue).	32
2.24	Energy transfer ratio from initial bending energy to translational kinetic energy of jumping hoops off water. The symbols are the same as those in Fig. 2.23.	33
3.1	Sequence of a grasshopper (male <i>Shirakiacris shirakii</i>) jumping on an artificial stem (60 mm). (a) Captured image from record. (b) Displacement of body center in time. (c) Displacement of tip of the artificial stem in time. (d) Velocity of body center of grasshopper (open circles and leg extension rate (filled circles).	39
3.2	Basic mechanism of leg extension of grasshopper. (a) The femoral-tibial joint and muscle arrangement of hind leg (Bennet-Clark, 1975). (b) The schematic of thrust mechanism of hind leg. A indicates the axis of rotation, E the insertion of extensor tibia muscle, and F the insertion of flexor tibia muscle.	40
3.3	2-DOF model of grasshopper jumping on a flexible substrate.	40
3.4	Body axis angle with respect to the horizon at the moment of take off depending on the dimensionless muscle work and mass ratio of the insect and stem.	42
3.5	Dimensionless takeoff velocity of the insect with various muscle work and mass ratio for $L = 1$ and $\beta = 30^\circ$	43
3.6	Energy transfer ratio from insects muscle work to the kinetic energy of the insect at the moment of take off.	43
3.7	Initial angle of body axis β dependency of energy transfer ratio from insects muscle work to the kinetic energy of the insect at the moment of take off for $M = 1$ and $L = l_f/l$	44

LIST OF FIGURES

3.8	Femur length compared with tibia length $L = l_f/l$ dependency of energy transfer ratio from insects muscle work to the kinetic energy of the insect at the moment of take off for $M = 1$ and $\beta = 30^\circ$	44
3.9	Predicted efficiency of jumping of four species of grasshoppers compared with experimentally measured data. (Yellow green) <i>Acrida cinerea</i> , (olive green) <i>Atractomorpha lata</i> , (purple) <i>Oedaleus infernalis</i> , (red) <i>Shirakiacris shirakii</i> . The yellow dashed lines on the grasshopper images indicate the line of force.	46
3.10	(a) A water strider that rests and jumps on water. (b) Definition of various lengths.	48
3.11	(a) A water strider that rests and jumps on water. (b) Definition of various lengths.	49
3.12	Jumping of a water strider (male <i>Aquarius paludum</i> with a body mass of 36.8 mg and an average length of middle and hind legs of 22.1 mm). (a) A representative sequence of the jump of the water strider on the water surface. (b) Average dimple depth formed by the legs (open circles for middle legs, filled circles for hind legs) during the jump. (c) Vertical velocity of the body center v (open circles) and the average downward velocity of the four legs with respect to body center v_d (filled circles). (d) Height of the body center of the water strider during the jump.	50
3.13	Flexibility factor. A flexibility factor C of a long thin flexible cylinder as a function of the scaled length L_f . Circles correspond to the numerically calculated values of C ; the blue dashed line $C = (1 + 0.082L_f^{3.3})^{-1}$, and the red dashed line $C = (1.15L_f)^{-1}$. The blue dashed line is used in this study for $L_f < 1.5$	52

LIST OF FIGURES

3.14 Musculoskeletal structure of middle leg of a water strider. The image of anatomical images were originally published by Demar (Murphey, 1971). 54

3.15 Measured angles of a water strider jumping on water. 55

3.16 Comparison of the moment of maximum depth of dimple generation between middle and hind legs. The correlation between tm of middle and hind legs in each trial, resulting in the correlation coefficient $r = 0.943$, p-value = 0.0311, and $df = 28$ implying the synchronous motion of four legs. Empirical results from the jump characteristics of females (filled symbols) and males (unfilled symbols) of *G. latiabdominis* (circles), *G. gracilicornis* (triangles), and *A. paludum* (squares) are also plotted. Dashed line indicates the exact match between middle and hind legs, and solid line indicates the fitted regression line. 55

3.17 Model of leg locomotion of water strider. (a and b) Comparison of leg locomotion between the sinusoidal model and a real water strider. The solid lines correspond to the model and the circles correspond to the measurement from the movie shown in Fig. 3.12(a). (a) The average vertical distance between the body center and distal end of legs (l_v) across the leg rotation cycle. (b) The average downward velocity of four legs with respect to body center (v_d). 56

3.18 Theoretical sinking depth of a cylinder. The maximum deformation of the meniscus due to a thin rigid cylinder floating on a surface of the liquid, with the interfacial inclination ϕ and the displacement of cylinder h_{max} . The maximum displacement of the center of a thin rigid floating cylinder at the gas-liquid interface is modeled to be reached at an interfacial inclination ϕ of $\pi/2$ and the displacement of cylinder (h_{max}) of l_c 57

LIST OF FIGURES

- 3.19 (a) Prediction of stroke. Effect of the dimensionless angular speed of leg rotation ($\Omega L_t^{-1/2}$) on the dimensionless maximum dimple depth (H_m) across a range of the dimensionless downward stroke (L_s). Inset: the phase of leg rotation at which meniscus reaches maximum depth (at $t = t_m$; blue lines), and at takeoff (at $t = t_t$; black lines). (b) Prediction of vertical jumping velocity. Prediction of vertical takeoff velocity of water striders jumping on water as a function of $\Omega L_t^{-1/2}$ for various L_s through the jump modes of post-takeoff closing (blue solid lines), pre-takeoff closing (red solid lines), and meniscus breaking (black dashed dot lines). Empirical results from the jump characteristics of females (filled symbols) and males (unfilled symbols) of *G. latiabdominis* (circles), *G. gracilicornis* (triangles), and *A. paludum* (squares) are also plotted. The empirical values of water striders with $L_s \approx 3.5$ (circles) and $L_s \approx 7$ (squares) are given. 60
- 3.20 Different jump modes. (a) Schematic representation of three modes of jump: pre-takeoff closing, post-takeoff closing and meniscus breaking jump. (b and c) Magnified images of the leg and dimple in a post-takeoff closing jump ($h_m = 2.5$ mm) and a meniscus breaking jump ($h_m > 3.9$ mm): (b) the leg that does not reach the sinking depth leaves the surface unpenetrated, (c) the leg pierces the surface just below the sinking depth. The red arrow at 3 ms indicates the rupture point of the water surface. The pre-takeoff closing jump was not observed in the experiments. 61
- 3.21 Comparison of vertical velocity. Experimentally measured, dimensionless vertical velocity of water striders versus theoretical predictions at the moment of maximum dimple depth (red symbols) and at takeoff (black symbols). Dashed dot line indicates the exact match between experiment and theory. The symbols are the same as those in Fig. 3.8. 61

LIST OF FIGURES

3.22	Phase diagram for the three jump modes (as a function of $\Omega L_t^{-1/2}$ and L_s): post-takeoff closing (white area), pre-takeoff closing (light shaded area), and meniscus breaking (dark shaded area). The red line marks the conditions resulting in maximal vertical takeoff velocity. Empirical results from the jump characteristics of females (filled symbols) and males (unfilled symbols) of <i>G. latiabdominis</i> (circles), <i>G. gracilicornis</i> (triangles), and <i>A. paludum</i> (squares) are also plotted.	62
3.23	A bent leg of a water strider pushing the water surface. The tapered leg keeps its tip pointing upward during the stroke, helping to prevent the rupture of meniscus. The time gap between each snapshot is 3 ms and the scale bar indicates 5 mm.	65
3.24	Force per unit length on the four legs of four water striders estimated from measured dimple depth and wetted length. The time is set to be zero when the maximum force is generated.	65
3.25	The relation between maximum capillary force $F_s = 4\gamma(L_1 + L_2 + L_3)$ and body weight of 342 species of water striders. The solid line describes the critical condition where the body weight becomes the same as maximum capillary force. The dashed dot line means the isometry condition with $F_s \sim F_g^{1/3}$. The dashed line shows the best fit to the data given by $F_s = 48F_g^{0.58}$, which has similar order to relation of the leg length and body mass based on our model. Originally published by Hu et al. (Hu <i>et al.</i> , 2003).	68
4.1	The equivalent model of water when capillary force is dominant.	71
4.2	The equivalent model of water when drag force is dominant.	71

LIST OF FIGURES

- 4.3 The efficiency of jump on deformable substrates of two degree of freedom system of a pair of jumper and basal hoops (*a*) without and (*b*) with damping effect. (Blue shade) water striders jumping on water, (green shade) grasshoppers jumping on artificial stem , and (orange shade) hoops on water. 72

Chapter 1

Introduction

One of the most attractive phenomena to engineers is jumping of small creatures. Some species show exceptional jumping performance reaching up to the height of hundreds times their body (Bennet-Clark, 1975; Bennet-Clark & Lucey, 1967; Brackenbury & Hunt, 1993; Burrows, 2003; Heitler, 1977; Sutton & Burrows, 2011). Invertebrates have developed different organs to fulfill their characterful functions, and jumping is one of the functions widely adopted. Diverse arthropods show various structures and function associated with jump. Many of them have advantage from long legs or wing movement to extend the propulsion time or gain additional thrust before takeoff (Burrows, 2013; Burrows & Wolf, 2002), whereas some have polished special skills with specialized triggering mechanisms, such like fleas (Bennet-Clark & Lucey, 1967), grasshoppers (Bennet-Clark, 1975; Heitler, 1977; Heitler & Burrows, 1977a,b), froghoppers (Burrows, 2003, 2006), and click beetles (Evans, 1972). There have been numerous achievement in research on jumping arthropods on land, and many attempts to mimicking jumping mechanism of them have been made and succeeded. However, all most of research on jump of remarkable arthropods have been limited to that on rigid solids, though these natural outstanding jumpers spend considerable time on vegetation.

Ribak et al. (Ribak *et al.*, 2012) reported that click beetles diminishing jumping performance on compliant substrates, and then concluded that

the click beetles jump to right their body upside-down when they were overturned. Click beetles have developed a unique jumping mechanism with the latch inside dorsal mesothorax, so that they jump up by the movement of mesothorax and metathorax (Evans, 1972) which seemingly does not serve any adjustment mechanism during jumping. In contrast, grasshoppers have highly developed hind legs not only strong but also easy to control as a main locomotor unlike click beetles. Regarding this point, we address how grasshoppers adjust their locomotion according to the substrate where they launch. The fundamental understandings of the exceptionally motility of grasshoppers on natural substrates would serve meaningful guide to small scale robots exploring the wild.

In nature, there are also various small creatures living on water; some of them jump fast even on water. In recent decades, their fascinating biolocomotion on water has been attracted many researchers (Hu *et al.*, 2003; Keller, 1998). It is widely known that small living creatures exploit capillary force to float and propel on the water surface (Hu *et al.*, 2003; Vella, 2008), in addition, their superhydrophobic legs ease overcome adhesion or friction with the water surface (Feng *et al.*, 2007; Lee & Kim, 2009). Nevertheless the general mathematics of momentum gained from surface locomotion including rowing and jumping on water have suggested (Hu & Bush, 2010; Vella & Metcalfe, 2007), it is too elementary level and not enough to extract essential insight about semi-aquatic locomotion or to be directly applied to develop devices mimicking the motility. In this study, we reveal how they exploit the water surface, the essential parameter of arthropods locomotion, and how we achieve fast takeoff on water.

This thesis would suggest clear understandings of jumping on natural substrates of small creatures which remains ambiguous yet, and directly applicable guides to building devices.

Chapter 2

Bio-inspired jumping hoops on various substrates

2.1 Introduction

Jumping is used by animals as an efficient means of locomotion to escape predators, to catch prey, to increase their speed, or to launch into flight (Burrows, 2003). Small insects such as froghoppers (Burrows, 2003, 2006), crickets (Burrows & Morris, 2003), fleas (Bennet-Clark & Lucey, 1967), grasshoppers (Bennet-Clark, 1975) and water striders (Hu & Bush, 2010; Lee & Kim, 2008) are able to jump many times their body lengths. Their jumps are powered by muscles that rapidly release stored elastic energy through a latch mechanism (Gronenberg, 1996). The major research foci of the field have been on the anatomical structure of organs associated with jumping (Burrows, 2006; Heitler, 1974; Rothschild *et al.*, 1975), the jump kinematics (Burrows & Morris, 2003; Burrows & Sutton, 2012; Burrows & Wolf, 2002), and the power exerted by the muscle that drives the jumps (Bennet-Clark, 1975; Evans, 1972).

Interest in the jumping of small objects is increasing outside biology. Inspired by the superior maneuverability of those insects, biomimetic robots, which mimic the structures, functions and designs of living creatures, are being developed with the goal to jump on land (Sugiyama & Hirai, 2006)

2.2 Jumping of an elastic hoop on a rigid solid

and water (Shin *et al.*, 2008). Optimizing the robot design to maximize the jump height is essential, given the constraints on material properties, size, and weight.

In contrast, the jump dynamics of small elastic objects have drawn little interest so far (Sutton & Burrows, 2011). In this paper, we analyze the dynamics of a model jumper, an elastic hoop, because of its simple geometry, ease of fabrication, and immediate implications for biomimetic robots (Sugiyama & Hirai, 2006). Circular-shaped robots have many advantages such as their structural stability and superior terrestrial mobility. Despite the long history of studying the dynamics of thin and thick hoops (Hobbs, 1965; Hoppe, 1871; Kirkhope, 1977; Love, 2013; Raux *et al.*, 2010), the jumps of the hoop have been seldom treated from a strictly mechanical point of view. As a consequence, questions regarding the energy efficiency of the jumps of the hoop (the ratio of the translational kinetic energy to the initially stored strain energy) and the amount of energy wasted due to the interaction with the substrate, the hoop vibration, and the effects of air drag are still unanswered. We address these questions and obtain the maximum jump height and the optimum design by a combination of experiments and the theory of elasticity. We also compare the effect of different substrates on jumping performance, such as rigid solid, flexible solid, and liquid.

2.2 Jumping of an elastic hoop on a rigid solid

A circular hoop resting on the substrate is bent by a sharp tip that is rapidly pulled back horizontally by a spring to let go of the hoop without interfering with its motion. Upon the release, the hoop starts to recover its circular shape while maintaining contact with the substrate ($t = 0-5$ ms) as shown in Fig. 2.1. It disengages from the substrate upon reaching a perfect circle ($t = 5$ ms). While in the air, the hoop vibrates between oblate and prolate shapes. Through measuring the maximum height reached by the hoops, H , with various radius R , thickness c , and initial deflection δ , we

2.2 Jumping of an elastic hoop on a rigid solid

found that the hoop jumps higher with the decrease of the radius and the increase of the thickness and the initial deflection.

2.2.1 Experimental methods

To measure the jump height of an elastic hoop off a rigid substrate, we made hoops of steel (SK5 carbon steel) with Young's modulus $Y=196$ GPa, density $\rho = 8.00 \times 10^3$ kg/m³, and yield stress $\sigma_y=612$ MPa. We also used polyimide films (Dupont Kapton) with $Y=3.55$ GPa, $\rho=1420$ kg/m³, and $\sigma_y=69.0$ MPa. The thickness c of the hoop ranges between 75 and 125 μm , and the radius (the average of the inner and outer radius in the undeformed state) R is between 10 and 30 mm; the width is fixed to $w=3$ mm (see Fig. 2.2(a)).

We tested glass, acrylic, and aluminum and found that the jumps of the hoops are insensitive to the rigid substrate material (the maximum jump height differed by at most $\pm 1\%$ depending on the material). In this chapter, all data for rigid solid are the result on a glass substrate. A circular hoop resting on the substrate is bent by a sharp tip which is rapidly pulled back horizontally by a spring to let go of the hoop without interfering with its motion (see Fig. 2.2(b)).

We visualized the resulting motion of the hoop using a high-speed camera (Photron FASTCAM APX-RS) at the frame rate 3000 s^{-1} . The location and shape of the hoop were obtained by digitizing the image, which consists of 512×720 pixels. The object size is calibrated by imaging a ruler with the identical imaging setup.

In this study, drag coefficient C_D of the hoops with different dimensions and velocity in water is obtained by measuring the drag force of each hoop moving steadily by a linear stage (Newport M-IMS300LM) with a load cell (HBM SP1). It is recalled that C_D is a function of Re and geometry only, not the kind of fluid (Batchelor, 1967).

2.2 Jumping of an elastic hoop on a rigid solid

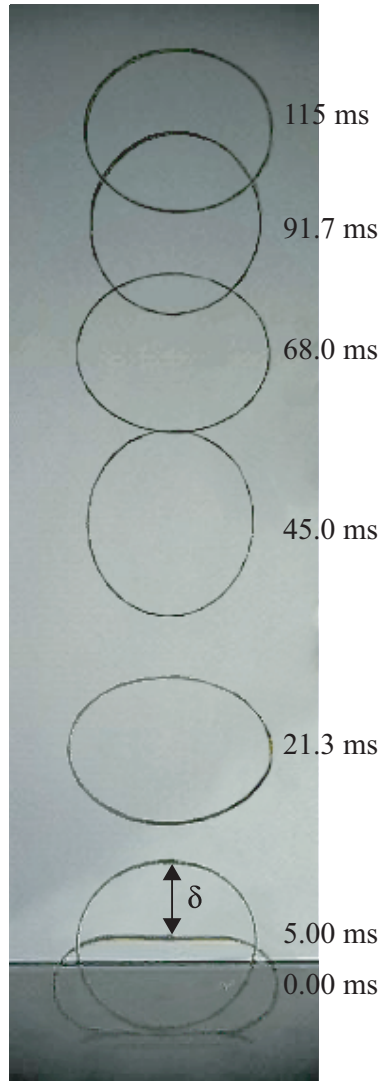


Figure 2.1: The jumping sequence of a hoop with radius $R = 16$ mm, width $w = 3$ mm, thickness $c = 125 \mu\text{m}$ and initial deflection $\delta = 14$ mm.

2.2 Jumping of an elastic hoop on a rigid solid

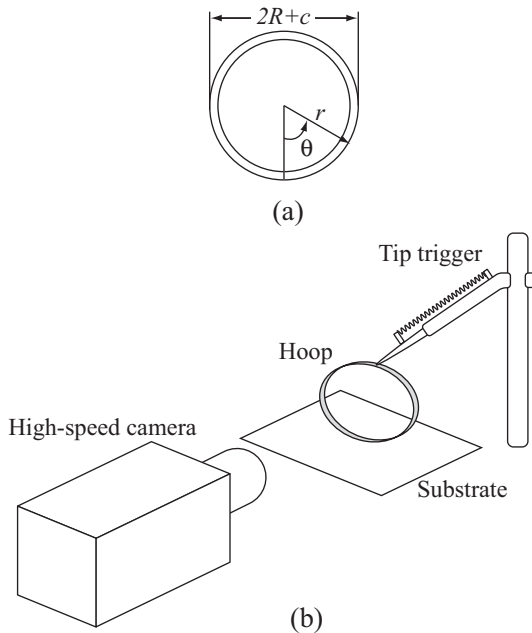


Figure 2.2: (a) The geometry of an elastic hoop. (b) The experimental apparatus for hoop jumping on flexible solid.

2.2.2 Jumping height without air drag

We first consider how the initial elastic strain energy due to bending, E_b , is consumed when the hoop jumps. Upon release, the hoop's elastic energy is partially imparted to the substrate, the amount of which is denoted by E_s . The rest is used to set the hoop in motion. Two different modes of the hoop motion occur: translation and vibration. Therefore, we may write the following relation for energy conservation: $E_b = E_s + E_{t,0} + E_{v,0}$, where $E_{t,0}$ and $E_{v,0}$ respectively indicates the initial translational and initial vibrational kinetic energy. $E_{t,0}$ is converted to three different forms of energy in the course of ascent, i.e. the instantaneous translational energy E_t , the gravitational potential energy $E_g = mgh$, and the energy loss due to air drag E_d . Here m and h is the mass and the instantaneous height of the hoop, respectively, and g is the gravitational acceleration. At the highest point the hoop reaches, where $E_t = 0$ and $h = H$, the energy conservation can be written as $E_b = E_s + E_g + E_d + E_{v,0}$.

2.2 Jumping of an elastic hoop on a rigid solid

The elastic strain energy of a hoop can be given by a linear relation (Love, 2013) between the compressive force F and the resulting deformation δ : $F = k\delta$, where $k = \eta Y w c^3 / R^3$ with $\eta = \pi / [3(\pi^2 - 8)] = 0.56$. Then we get $E_b = \frac{1}{2} k \delta^2 = 0.28 Y w c^3 \delta^2 / R^3$. By measuring F and δ , we find this linear relation to hold well beyond the geometrically linear regime (i.e. small deformations compared to the hoop length) until the upper and lower segments of the hoop touch each other, i.e. $\delta = 2R - c$. To find the energy associated with the motion of the hoop, we write the velocity of the thin hoop as $\mathbf{U}(\theta, t) = U_c(t)\mathbf{k} + \mathbf{U}_r(\theta, t)$, where U_c is the speed of the center of mass (CM), \mathbf{k} the unit vector in the vertical direction, and \mathbf{U}_r is the velocity of a point in the hoop with respect to the CM. For the coordinate system, see Fig. 2.2(a). The initial translational energy

$$E_{t,0} = \frac{1}{2} m U_c^2(0), \quad (2.1)$$

where $t = 0$ indicates the moment of takeoff. The initial vibration energy $E_{v,0} = \frac{1}{2} \int U_r^2(\theta, 0) dm$. Since the hoop exhibits up-down symmetry in vibration upon takeoff and is circular at $t = 0$, we write $\mathbf{U}_r(0, 0) = -U_c(0)\mathbf{k}$ and $\mathbf{U}_r(\pi, 0) = U_c(0)\mathbf{k}$. For a thin ring freely vibrating in a plane in its second mode, the radial displacement u and the circumferential displacement v are respectively given by $u(\theta, t) = -2B \cos 2\theta \cos(\omega_n t + \epsilon)$ and $v(\theta, t) = B \sin 2\theta \cos(\omega_n t + \epsilon)$, where B is the vibration amplitude, ω_n the natural frequency and ϵ the phase adjustment (Love, 2013). Then $U_r = (\dot{u}^2 + \dot{v}^2)^{1/2} = B\omega_n(4 \cos^2 2\theta + \sin^2 2\theta)^{1/2} \cos(\omega_n t)$, where the dot denotes the time derivative. Using $U_r(\pi, 0) = 2B\omega_n = U_c(0)$, we get

$$E_{v,0} = \frac{5}{16} m U_c^2(0). \quad (2.2)$$

Because the vibration speed of a hoop $U_r \sim \omega_n \delta$, where \sim denotes “is scaled as”, $\omega_n \sim (Y/\rho)^{1/2} c/R^2$ Hoppe (1871) and $U_r \sim U_c$ at takeoff, both $E_{t,0}$ and $E_{v,0}$ are scaled with $Y w c^3 \delta^2 / R^3$ just as E_b . Furthermore, $E_{v,0}/E_{t,0}$ has a constant ratio, $\frac{5}{8}$, owing to Eqs. (2.1) and (2.2). Our experimental measurements on the positions of the top and bottom of the hoop versus time reveal that $E_{t,0} \approx 0.57 E_b$, as shown in Fig. 2.3, the proportionality

2.2 Jumping of an elastic hoop on a rigid solid

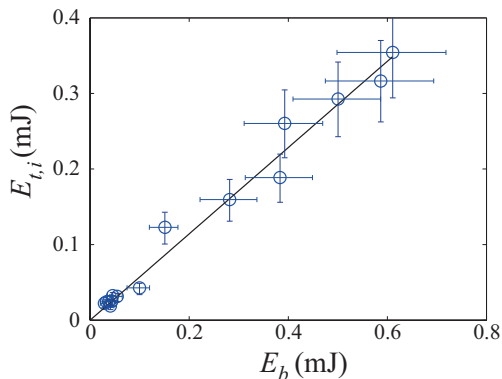


Figure 2.3: Experimental measurement results for the initial translational kinetic energy $E_{t,0}$ and elastic strain energy E_b , showing a linear relationship between them. The slope of the best fitting line is 0.57.

constant being slightly less than $\frac{8}{13} \approx 0.62$ due to energy loss to the substrate. It follows that $E_{v,0} = \frac{5}{8}E_{t,0} \approx 0.36E_b$ because Eqs. (1) and (2), and $E_s \approx 0.07E_b$ by energy conservation. That is, approximately 57% and 36% of the initial elastic strain energy is converted to the translational and vibrational energy at take-off, respectively, and the remaining 7% is dissipated in the interaction with the substrate. Although we started with a thin ring approximation ($c/R \ll 1$), the vibrational energy of a thick ring was shown (Kirkhope, 1977) to be proportional to the initial strain energy up to $c/R \approx 0.5$, to which point our model can be extended.

Now we can get a crude scaling law for the jumping height by balancing $E_{t,0} \sim Ywc^3\delta^2/R^3$ with the maximum gravitational potential energy mgH :

$$\frac{H}{h_c} \sim \frac{c^2\delta^2}{R^4}, \quad (2.3)$$

where we used $m = 2\pi\rho Rcw$ and $h_c = Y/\rho g$ having the dimension of lengths. Figure 2.4 shows the experimental data plotted according to the scaling law (2.3) with a straight line obtained by letting $E_{t,0} = 0.57E_b = mgH$. We see that the discrepancy between theory and experiment grows as H increases, which is due to the energy loss caused by air drag.

2.2 Jumping of an elastic hoop on a rigid solid

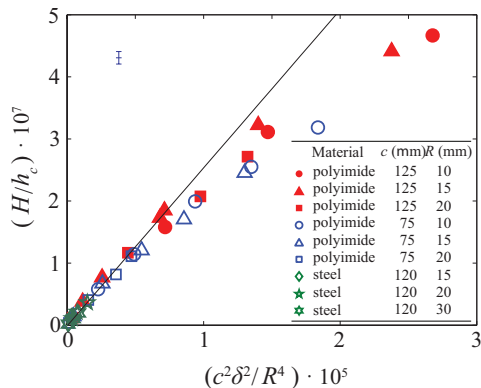


Figure 2.4: (Color online) The maximum jumping heights of various hoops with δ ranging up to 12 mm plotted according to the scaling law: $H/h_c \sim c^2 \delta^2 / R^4$. The straight line corresponds to the jumping height with no air drag obtained by letting $E_{t,0} = 0.57 E_b = mgH$. Characteristic error bars are shown in the upper left corner.

2.2.3 Jumping height with air drag

We consider an equation of motion of the hoop in the vertical direction:

$$m\dot{U}_c = -mg - D, \quad (2.4)$$

where the drag $D = C_D \rho_a R w U_c^2$. Here C_D is the drag coefficient and ρ_a is the air density. It is recalled that C_D is a function of Re and geometry only, not the kind of fluid (Batchelor, 1967).

We found that over a Reynolds number range, $\text{Re} = U_c w / \nu$ (150 – 1500), ν being the kinematic viscosity, which corresponds to the current experimental conditions, C_D is a constant of 2.32 for all the hoops satisfying $c/R < 0.04$. As the hoop thickness further increases, C_D tended to decrease, in which case a separate measurement of C_D is required. Except for the variation of the numerical values of C_D , our theory (i.e. all the relations given in the manuscript) holds up to $c/R \approx 0.5$.

By integrating Eq. (2.4), the hoop velocity $U_c(t)$ is given by

$$U_c(t) = \sqrt{h_D g} \tan \left(\tan^{-1} \frac{U_0}{\sqrt{h_D g}} - \frac{t}{\sqrt{h_D/g}} \right), \quad (2.5)$$

2.2 Jumping of an elastic hoop on a rigid solid

where $U_0 = U_c(0)$. Integrating $U_c = \dot{h}$ with $h(0) = 0$, we get

$$h(t) = h_D \ln \frac{\cos \left[\tan^{-1} (U_0/\sqrt{h_D g}) - t/\sqrt{h_D/g} \right]}{\cos \left[\tan^{-1} (U_0/\sqrt{h_D g}) \right]}, \quad (2.6)$$

where $h_D = 2\pi\rho c/\rho_a C_D$. The initial hoop velocity is related to ω_n and δ , and we experimentally found $U_0 \approx 0.232(Y/\rho)^{1/2}c\delta/R^2$. The maximum height of the hoop jump under the effect of air drag, H_a , is obtained by substituting $t = t_{max} = \sqrt{h_D/g} \tan^{-1} (U_0/\sqrt{h_D g})$, which makes $U_c(t_{max}) = 0$, into Eq. (2.6):

$$H_a = -h_D \ln \left| \cos \left[\tan^{-1}(0.232\sqrt{\phi}) \right] \right|, \quad (2.7)$$

where $\phi = (h_c/h_D)(c^2\delta^2/R^4)$. We note that the dimensionless maximum height H_a/h_D depends on a single parameter ϕ , which can be shown to be $\phi \sim D_0/mg$, where $D_0 = C_D\rho_a R w U_0^2$. Figure 2.5 shows that the model can accurately predict the temporal evolution of the hoop height. Figure 2.6 shows that our model can collapse all the experimental data for maximum height on to a single line with a single parameter ϕ . The energy loss due to air drag can be evaluated as $E_d = mg(H_m - H_a)$, where H_m is the maximum jump height with no air drag. Substituting $E_{t,0}$ above into $H_m = E_{t,0}/mg$, we get $H_m \approx 0.026h_c c^2 \delta^2 / R^4$, which can also be derived by taking $C_D \rightarrow 0$ in Eq. (2.7) because $\ln \left| \cos \left[\tan^{-1}(0.232\sqrt{\phi}) \right] \right| \approx 0.026\phi$ for $\phi \ll 1$.

We plot the energy ratio $E_d/E_{t,0} = 1 - H_a/H_m$ and $E_g/E_{t,0} = H_a/H_m$ versus ϕ in Fig. 2.7. The results of $E_d/E_{t,0}$ increasing and $E_g/E_{t,0}$ decreasing with ϕ are intuitively obvious considering that ϕ corresponds to the ratio of the drag to the weight.

2.2.4 Optimization of hoop geometry

We now turn to the optimization of the hoop design and the degree of deformation to maximize the jumping height H_a in air for a given mass of a hoop material. Here we emphasize that thanks to the simple formula for H_a , Eq. (2.7), the optimization is reduced to a simple algebraic problem, without which a time-consuming numerical computation would be required.

2.2 Jumping of an elastic hoop on a rigid solid

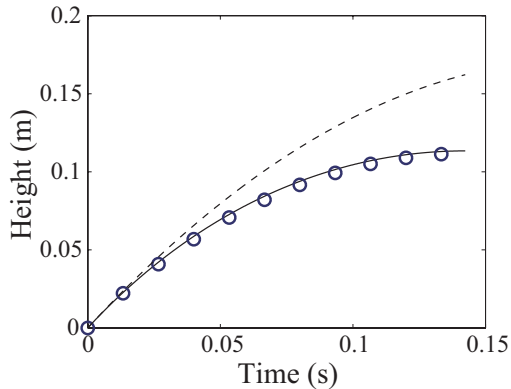


Figure 2.5: Experimentally measured temporal evolution of the height of the hoop with radius $R = 15$ mm, thickness $c = 125$ μm and initial deflection $\delta = 9$ mm (circles) compared with the theories neglecting (dashed line) and considering (solid line) the air drag. Characteristic error bars are shown in the lower right corner.

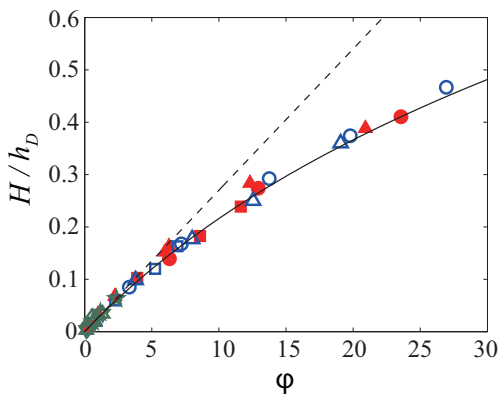


Figure 2.6: Dimensionless maximum jumping height versus ϕ . The solid line is from Eq. (2.7) and the broken line is drawn by taking $C_D \rightarrow 0$ in Eq. (2.7). Characteristic error bars are shown in the lower right corner.

2.2 Jumping of an elastic hoop on a rigid solid

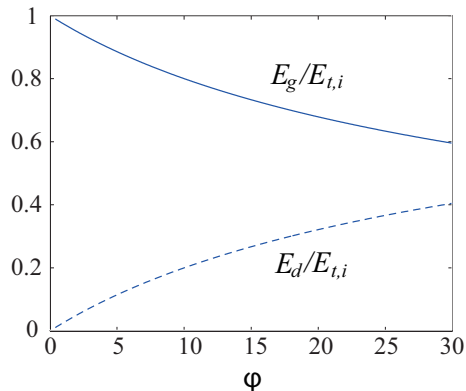


Figure 2.7: The energy conversion ratio from $E_{t,0}$ to E_g (solid line) and to E_d (dashed line).

We can show that H_a in Eq. (2.7) depends upon only two parameters, c/R and δ , when Y , w and $m = 2\pi\rho Rwc$ are fixed. Because $\partial H_a/\partial(c/R)|_\delta > 0$ and $\partial H_a/\partial\delta|_{c/R} > 0$, always, maximizing both c/R and δ under specific constraints will maximize H_a . Here we choose three constraints. The first constraint is given by hoop geometry: $\delta < 2R - c$, which can be expressed as

$$\delta < (Rc)^{1/2} \left(\frac{c}{R}\right)^{-1/2} \left(2 - \frac{c}{R}\right), \quad (2.8)$$

where we fix Rc . To prevent the yield of the material, we choose the second constraint as $\sigma_m \leq \sigma_y$, where the maximum stress in the hoop $\sigma_m = F[6 + 38(b/a)^2]/(\pi awR)$ that occurs at the intersection of the inner circumference and the line of action of diametrical load and σ_y is the yield stress Hoppe (1871). Then δ can be written as

$$\delta < \frac{\pi}{1.12} \frac{\sigma_y \sqrt{Rc}}{Y} \left(\frac{R}{c}\right)^{7/2} \frac{a}{3 + 19(b/a)^2}, \quad (2.9)$$

where $a = 1 + \frac{1}{2}c/R$ and $b = 1 - \frac{1}{2}c/R$. Since a device that bends the hoop, e.g. the leg muscle of an insect or an actuator of a robot, can exert a finite force $F \leq F_m$, the third constraint is given by

$$\delta < \frac{F_m}{0.56Yw(c/R)^3}. \quad (2.10)$$

2.2 Jumping of an elastic hoop on a rigid solid

Because all the three constraints give the maximum allowable δ as the functions of c/R , a single parameter c/R can be tuned to optimize H_a in Eq. (2.7).

Figure 2.8, and 2.9 shows the examples of the optimization results using the hoops of (a) steel and (b) polyimide. We set $F_m = 1.5$ N and 0.1 N, $Rc = 6 \times 10^{-6}$ m² and 2×10^{-6} m² for (a) and (b), respectively, to restrict the jumping height within the laboratory space. For both the cases, the relations (2.8) and (2.10) define the maximum jump height for varying c/R owing to the high strength of the materials. For a point designated as A in Figs. 2.8, and 2.9, the hoop can be initially compressed until its upper segment touches the lower one while still satisfying conditions (2.9) and (2.10). For point C, the hoop can be initially bent up to a point where the compression force reaches F_m . Point B, where the conditions (2.8) and (2.9) coincide, gives the greatest jump height thus the optimal value of c/R . Figure 2.8, and 2.9 also shows that our experiments agree well with the theory.

The jumping of an elastic hoop was analyzed through a combination of experiment and theory. A remarkable finding is that a constant portion (57%) of the initial elastic strain energy, independent of the thickness, radius, initial deflection, and material properties of the hoop, is used to raise the hoop provided that $c/R < 0.5$ and the initial gravitational sagging is ignored. Considering the effects of drag, we find that the jump height H nondimensionalized by h_D (see Eq. 2.6) is a function of a single parameter ϕ (see Eq. 2.7) that corresponds to the ratio of the initial air drag to the weight. When a hoop mass of a given material is given, the optimal condition to achieve the maximum jump height is determined by a single parameter c/R , i.e. the ratio of the thickness to the radius of a hoop. In this work, we used a constant value of the drag coefficient $C_D = 2.32$ for a fixed hoop width w , which is experimentally verified to be valid for $c/R < 0.04$. For the thicker hoops, C_D was observed to decrease, which can result in a greater jump height than predicted. The optimal value of c/R , however, is not affected by the value of C_D .

2.2 Jumping of an elastic hoop on a rigid solid

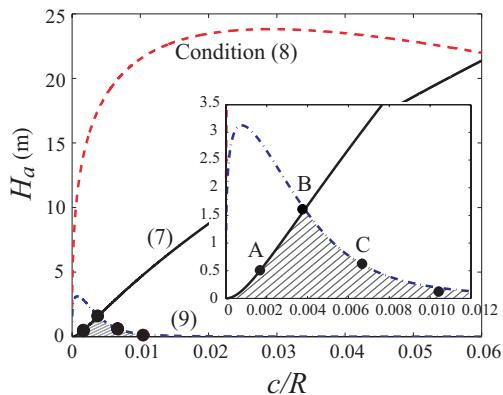


Figure 2.8: Maximum jumping heights H_a (in air) versus c/R predicted by Eq. (2.7) that correspond to the conditions of Eqs. (2.8) (solid line), (2.9) (dashed line), and (2.10) (alternate long and short dash line). All the three conditions are met in the hatched area. Filled circles are experimental results. Steel hoops. Inset: Magnified view around the optimum. A: initially the upper segment of a hoop touches the lower one, but the compression force is lower than the maximum allowable actuator force F_m . B: initially the hoop bends until its upper segment touches the lower one, at which state the compression force reaches F_m . C: the hoop is compressed with the maximum allowable actuator force F_m , but the upper segment does not touch the lower one.

2.2 Jumping of an elastic hoop on a rigid solid

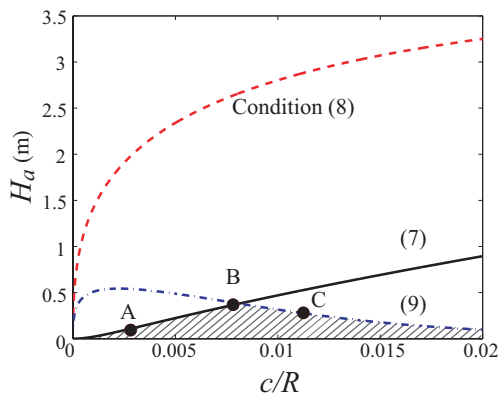


Figure 2.9: Maximum jumping heights H_a (in air) versus c/R predicted by Eq. (2.7) that correspond to the conditions of Eqs. (2.8) (solid line), (2.9) (dashed line), and (2.10) (alternate long and short dash line). All the three conditions are met in the hatched area. Filled circles are experimental results. Polyimide hoops. A: initially the upper segment of a hoop touches the lower one, but the compression force is lower than the maximum allowable actuator force F_m . B: initially the hoop bends until its upper segment touches the lower one, at which state the compression force reaches F_m . C: the hoop is compressed with the maximum allowable actuator force F_m , but the upper segment does not touch the lower one.

2.3 Jumping of an elastic hoop on flexible solids

The analytical framework for the dynamics of the model jumper constructed here enables us to start thinking about jumping of various other geometries such as slender beams and hollow shells. In particular, a topic of biophysical interest would be the shape and dimension of a semilunar process, consisting of chitin fibers in a protein matrix (Shewry *et al.*, 2003), which is responsible for storing the elastic energy in the legs of jumping insects such as a locust (Burrows & Morris, 2001), to see whether it has evolved to maximize the jumping efficiency. Also the jumping behavior of various objects on a flexible substrate, which will certainly dissipate more than 7% of the initial elastic energy that a rigid one does, is worth study to understand insect jumps on plant leaves and on water (Brackenbury & Hunt, 1993; Hu & Bush, 2010; Lee & Kim, 2008).

2.3 Jumping of an elastic hoop on flexible solids

We tested glass, acrylic, and aluminum and found that the jumps of the hoops are insensitive to the rigid substrate material (the maximum jump height differed by at most $\pm 1\%$ depending on the material). In contrast, when the substrates are very soft such as a flexible polymer membrane, the deformation of the substrate has a great influence on the dynamics of the hoop. To observe the jump of an elastic hoop on flexible substrates, we chose similar elastic hoops as the flexible substrates.

A circular hoop resting on the supporting hoop is bent beforehand and tied by thin thread which is cut by a laser beam to let go of the hoop with negligible interfering with its motion. After release, the hoop starts to recover its circular shape while pushing down the supporting hoop and then disengages from the substrate. While in the air, the hoop vibrates between oblate and prolate shapes, at the same time, the supporting hoop also vibrates.

2.3 Jumping of an elastic hoop on flexible solids

2.3.1 Experimental methods

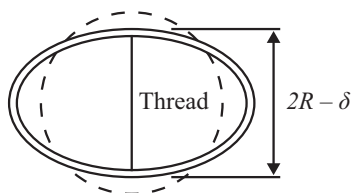
To observe the jump of an elastic hoop on flexible substrates, we chose similar elastic hoops as the flexible substrates. We made both jumping and supporting hoops of polyimide films (Dupont Kapton) with $Y=3.55$ GPa, $\rho=1420$ kg/m³, and $\sigma_y=69.0$ MPa; and steel (SK5) with $Y=196$ GPa, $\rho=8000$ kg/m³, and $\sigma_y=612$ MPa. The thickness c of the hoop ranges between 75 and 125 μm , and the radius (the average of the inner and outer radius in the undeformed state) R is between 10 and 50 mm; the width of jumping and supporting hoops are fixed to $w=3$ mm and 10 mm, respectively (see Fig. 2.10).

A circular hoop resting on the substrate is bent beforehand and tied by thin thread which is cut by a laser beam to let go of the hoop with negligible interfering with its motion.

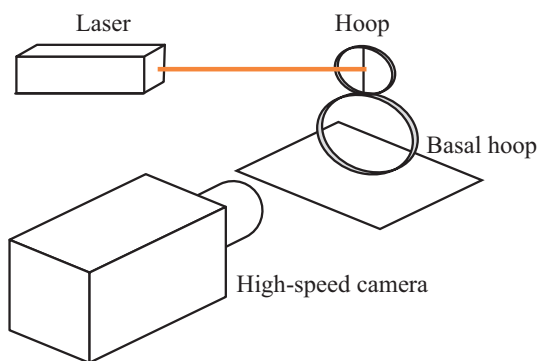
2.3.2 General features of jumping on basal hoops

Jump height of an elastic hoop initially storing a certain amount of energy varies depending on the substrates. Figure 2.11 shows the jumping height if four sets of hoops; first, a jumping hoop made of steel with radius 15 mm, width 3 mm, thickness 100 μm , and a basal hoop made of polyimide with radius 6 mm, width 6 mm, thickness 125 μm ; second, a jumping hoop made of steel with radius 20 mm, width 3 mm, thickness 100 μm , and a basal hoop made of polyimide with radius 6 mm, width 6 mm, thickness 125 μm ; third, a jumping hoop made of steel with radius 15 mm, width 3 mm, thickness 100 μm , and a basal hoop made of polyimide with radius 6 mm, width 12 mm, thickness 125 μm ; last, a jumping hoop made of steel with radius 20 mm, width 3 mm, thickness 100 μm , and a basal hoop made of polyimide with radius 6 mm, width 12 mm, thickness 125 μm . Dependency of the jumping height ratio of the basal hoop to rigid solids on the frequency ratio of a basal hoop and a jumping hoop shows a peak in the middle and the asymptotic value one when the frequency ratio increases infinitely large. The regime where the jumping height changes

2.3 Jumping of an elastic hoop on flexible solids



(a)



(b)

Figure 2.10: (a) The geometry of an elastic hoop. (b) The experimental apparatus for hoop jumping on a flexible solid.

2.3 Jumping of an elastic hoop on flexible solids

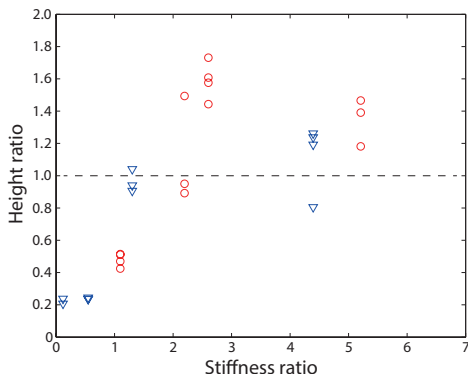


Figure 2.11: The jumping height of hoops on basal hoops. (Blue wedges) a jumping hoop made of steel with radius 15 mm, width 3 mm, thickness $100 \mu\text{m}$ on a basal hoop made of polyimide with various dimensions; (red circles) a jumping hoop made of steel with radius 20 mm, width 3 mm, thickness $100 \mu\text{m}$ on a basal hoop made of polyimide with various dimensions.

most sensitively to natural frequency ratio is those with the basal hoop with similar scale of natural frequency to the jumper. A slight difference in phase of two hoops can cause a significant different acceleration of the jumping hoop. Observed maximal jumping heights average about 1.6 times jumping height of that on rigid solids, which implies that almost all initial energy of the jumping hoop is transferred into translational kinetic energy or gravitational potential energy of the hoop.

Three different typical modes of jump, except for the jump on asymptotically stiff surface, were observed based on phase difference between a jumping and a basal hoop. These three modes can be defined as hindered jumping, assisted jumping, and ping-ponging mode, respectively. Hindered jumping mode means that the basal hoop keeps descending while the jumping hoop pushes down it, therefore, the takeoff velocity becomes much slower than jump on rigid solids (Fig. 2.12). Assisted jumping mode occurs when the basal hoop is much stiffer and has higher natural frequency than jumping hoop which implies the basal hoop is able to support the jumping hoop. The jumping hoop hardly deforms the basal hoop, but the basal hoop

2.3 Jumping of an elastic hoop on flexible solids

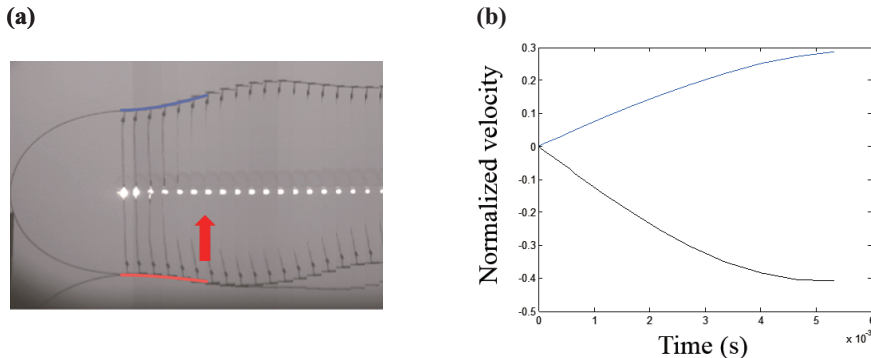


Figure 2.12: (a) The sequence of sliced images of hindered jumping mode ($K < 1, \Omega > 2.3$) with displacement prediction (blue and red solid lines). The time gap is 0.3 ms. (b) The velocity of top and bottom of the jumping hoop until take off. The jumping hoop made of polyimide with $R = 20$ mm, $c = 125 \mu\text{m}$, $w = 3$ mm, and $\delta = 5$ mm. The basal hoop made of polyimide with $R = 24$ mm, $c = 125 \mu\text{m}$, and $w = 3$ mm.

pushes upward when the jumping hoop takes off as shown in Fig. 2.13. The third mode occurs when the basal hoop is too weak and moves too slow to support the jumping hoop upward, so that the jumping hoop takes off too slow, leading to repetitive contact and detachment between two hoops was observed (Fig. 2.14).

2.3.3 Takeoff velocity of hoops on basal hoops

When a hoop takes off a rigid solid, the system would be modeled as a 1DOF mass-spring system. In contrast, a pair of jumper and basal hoops can be simply modeled as a vibrating system with two degree of freedom, because both top and bottom of the jumping hoop move. The series of ordinary differential equation can be written as below,

$$\ddot{x}_1 = \frac{k_1}{m_1}(x_2 - x_1), \quad (2.11)$$

$$\ddot{x}_2 = \frac{1}{m_2}[k_1(x_1 - x_2) - k_2x_2], \quad (2.12)$$

2.3 Jumping of an elastic hoop on flexible solids

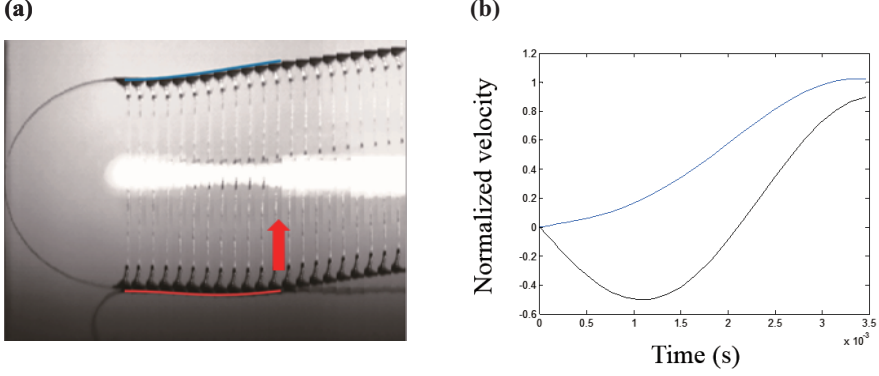


Figure 2.13: (a) The sequence of sliced images of assisted jumping mode ($K > 1, \Omega > 2.3$) with displacement prediction (blue and red solid lines). The time gap is 0.3 ms. (b) The velocity of top and bottom of the jumping hoop until take off. The jumping hoop made of steel with $R = 20$ mm, $c = 100 \mu\text{m}$, $w = 3$ mm, and $\delta = 3$ mm. The basal hoop made of polyimide with $R = 6$ mm, $c = 125 \mu\text{m}$, and $w = 12$ mm.

where, m and k mean the equivalent mass and stiffness of 2DOF system, respectively. And subscript 1, and 2 reflect the top of the jumping hoop and the contact point between the jumping and basal hoops, respectively. The equivalent mass of the oscillating hoop would be defined by the velocity of distributed infinitesimal masses at the instant. In this study, however, it is simplified in the two cases: the jumping hoop modeled as a single mass at the top (Fig. 2.16), or two identical masses at the top and bottom (Fig. 2.15). With a single mass jumper model, the equivalent mass of the hoop m_j would become $13/32$ of mass of the jumping hoop, the equivalent mass of the basal hoop m_b of $13/32$ times the basal hoop, and stiffness k_j , and k_b of the jumping and basal hoops in the same way of the jumping on a rigid solid, resulting in $m_1 = m_j$, $m_2 = m_b$, $k_1 = k_j$, and $k_2 = k_b$. On the other hand, 2DOF jumper model would be with m_j as $10/32$ times mass of the jumping hoop, resulting in $m_1 = m_j$, $m_2 = m_j + m_b$, $k_1 = k_j$, and $k_2 = k_b$. The initial condition are the initial position of two masses, $x_1(0) = -\delta$, $x_2(0) = 32/13 \times m_j g / k_b$, and the initial velocity of two masses,

2.3 Jumping of an elastic hoop on flexible solids

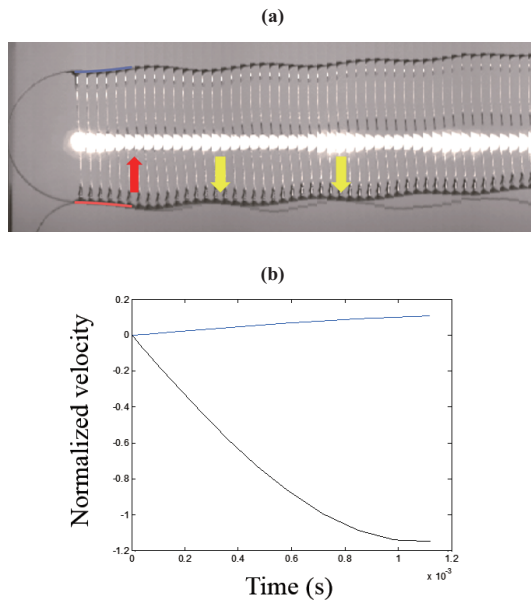


Figure 2.14: (a) The sequence of sliced images of ping-ponging mode ($K < 1, \Omega < 2.3$) with displacement prediction (blue and red solid lines). The time gap is 0.3 ms. Red arrow indicates takeoff, and yellow arrows direct bouncing. (b) The velocity of top and bottom of the jumping hoop until the first detachment. The jumping hoop made of steel with $R = 15$ mm, $c = 100 \mu\text{m}$, $w = 3$ mm, and $\delta = 2$ mm. The basal hoop made of polyimide with $R = 10$ mm, $c = 125 \mu\text{m}$, and $w = 3$ mm.

2.3 Jumping of an elastic hoop on flexible solids

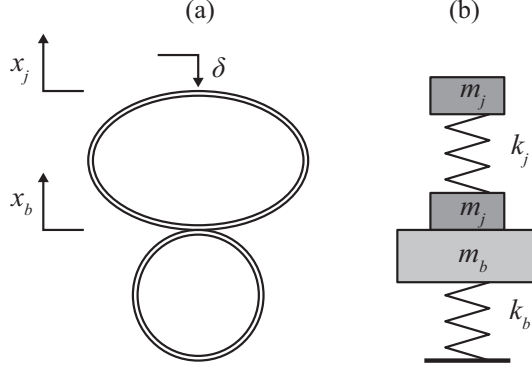


Figure 2.15: The two degree of freedom system of a pair of jumper with double masses model and basal hoops. Subscript 'j' indicates the jumper and 'b' refers to the basal hoop.

$$\dot{x}_1(0) = 0, \text{ and } \dot{x}_2(0) = 0.$$

These equations can be transformed into a pair of nondimensional differential equations,

$$\ddot{X}_1 = (X_2 - X_1), \quad (2.13)$$

$$\ddot{X}_2 = \frac{\Omega^{-2}}{K} [X_1 - (1 + K)X_2], \text{ or} \quad (2.14)$$

$$\ddot{X}_2 = \frac{1}{K\Omega^{-2}} [X_1 - (1 + K)X_2], \quad (2.15)$$

where $X = x/\delta$, $K = k_b/k_j$, and $\Omega = \omega_b/\omega_j$. With the initial condition with $X_1(0) = 1$ and other values set to zero, we can get the dynamics of the two hoops, leading to take off velocity of the jumping hoop. Equation 2.14 is for a single mass model of the jumping hoop, and eq. 2.15 is for a double mass model of the jumping hoop. The resulting takeoff velocity of the jumping hoop can be determined by the velocity of the jumping hoop at the moment of zero acceleration. Figure 2.17 shows the resulting takeoff velocity ratio with respect to the takeoff velocity on a rigid solid, which agrees well with the observed data. We can also see here the data of bouncing mode (blue circles) more faster than hoops taking off a rigid solid. A single mass jumper model is used when $K > 5$, while double masses jumper model is used when $K < 5$.

2.3 Jumping of an elastic hoop on flexible solids

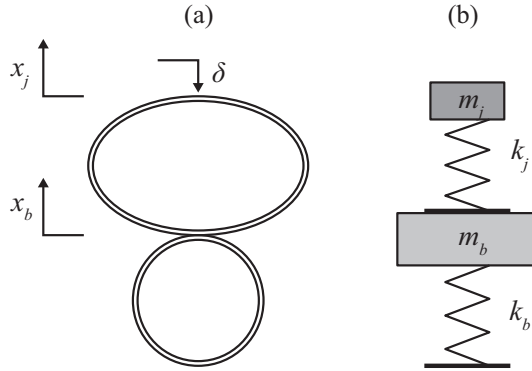


Figure 2.16: The two degree of freedom system of a pair of jumper with a single mass model and basal hoops. Subscript 'j' indicates the jumper and 'b' refers to the basal hoop.

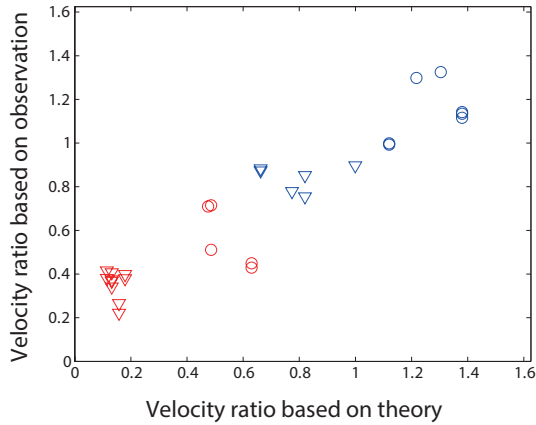


Figure 2.17: Take off velocity ratio of elastic hoops on basal hoops with respect to the jump on the rigid solid. Circles indicate the natural frequency ration of basal hoop to jumper larger than 2.3, wedges means that smaller than 2.3, red symbols means the stiffness ratio of basal hoop to jumper smaller than 1, and blue symbols indicate the ratio larger than 1.

2.4 Jumping of an elastic hoop on water

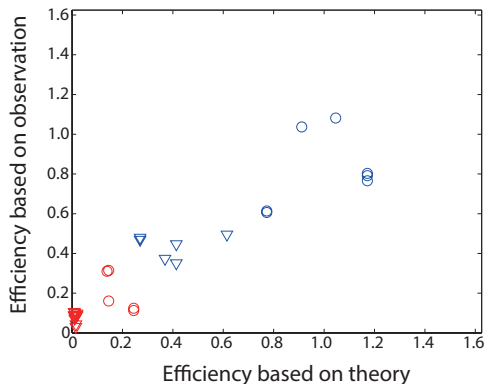


Figure 2.18: Jumping efficiency based on the take off velocity ratio of elastic hoops on basal hoops with respect to the jump on the rigid solid. Symbols are the same as Fig. 2.17.

2.3.4 Efficiency of jumping of hoops on basal hoops

The energy transfer ratio from initial bending energy of the jumping hoop to translational kinetic energy corresponding to the Fig. 2.17 is described in Fig. 2.18. The dependency of the jumping efficiency on natural frequency ratio and stiffness ratio between the basal hoop and the jumper is shown in Fig. 2.19. For $K < 5$, jumping efficiency drops near the frequency ratio of one. Efficiency gradually decreases with low frequency ratio, in contrast, the efficiency is saturated with higher frequency ratio than one. For $K > 5$, the efficiency is affected by the frequency ratio only with the higher frequency ratio than one. The map shows that the jumping on a basal hoop faster than that on a rigid solid is only possible with higher frequency ratio than two, and higher stiffness ratio than two.

2.4 Jumping of an elastic hoop on water

A circular hoop resting on the water surface initially bent and tied by a thin thread which is rapidly cut by a laser beam to let go of the hoop without significant interfering with its motion. After release, the hoop starts to recover its circular shape while pushing down the water surface

2.4 Jumping of an elastic hoop on water

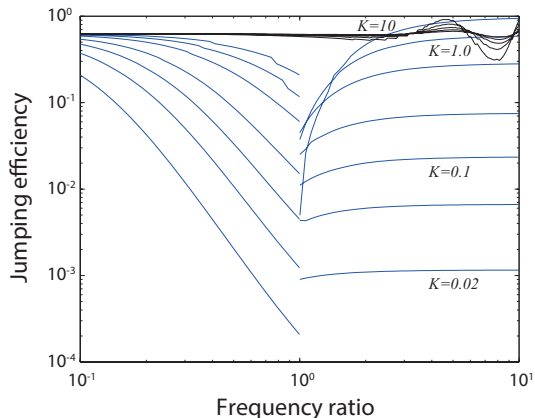


Figure 2.19: The dependency of the jumping efficiency on natural frequency ratio and stiffness ratio between the basal hoop and the jumper. (Blue lines) double masses jumper model is used for $K < 5$, (black lines) a single mass jumper model is used for $K > 5$.

($t = 0-16$ ms) (see Fig. 2.20). The impact of hoop on the water surface is maintained during the vertical lengthening of the shape and remains the dimple which slowly disappears and is followed by wave on the liquid surface. By measuring the maximum height H reached by the hoops for various values of hoop radius (R), hoop radius (c), and hoop radius (δ) we found that the hoop jumping efficiency, or energy transfer ratio from initial energy to translational kinetic energy of the hoop, substantially varies on the water surface unlike that on rigid solids. Our experiment show the hoop apparently jumps off water in the case of dynamic pressure dominant jump with $Re \sim 10^2 - 10^3$ and $We \sim 10^0 - 10^1$.

2.4.1 Experimental methods

To observe the jump of an elastic hoop on water, we made hoops of polyimide films (Dupont Kapton) with $Y=3.55$ GPa, $\rho=1420$ kg/m³, and $\sigma_y=69.0$ MPa, coated with super-hydrophobic particle of AKD (Alkylketene Dimer). The thickness c of the hoop ranges between 75 and 125 μm , and the radius (the average of the inner and outer radius in the undeformed

2.4 Jumping of an elastic hoop on water

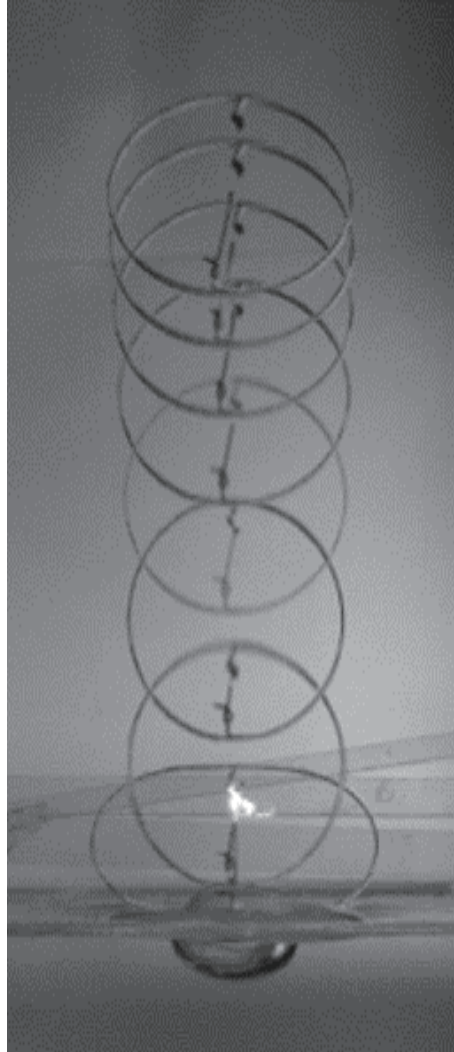


Figure 2.20: The overlapped images of jumping of a polyimide hoop with radius $R=10$ mm, thickness $c=125$ μm , and initial deflection $\delta=7$ mm on water.

2.4 Jumping of an elastic hoop on water

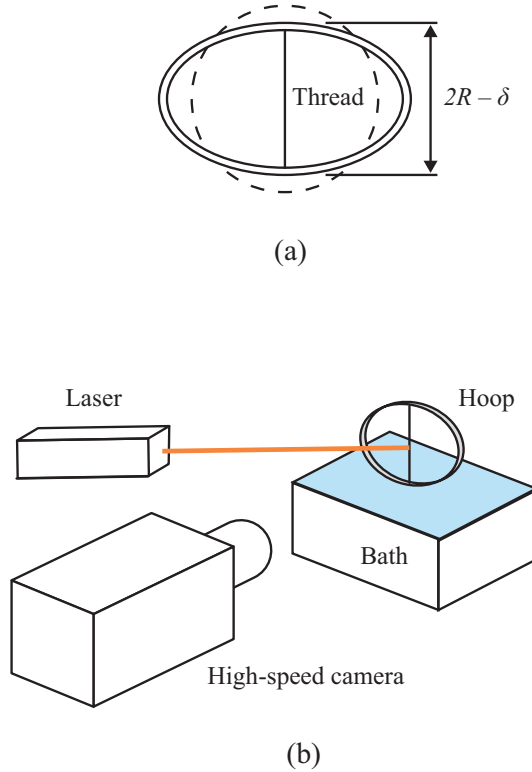


Figure 2.21: (a) The geometry of an elastic hoop. (b) The experimental apparatus for hoop jumping on water.

state) R is between 10 and 20 mm; the width of hoop is fixed to $w=1.5$ mm.

A circular hoop resting on liquid is bent beforehand and tied by thin thread which is cut by a laser beam to let go of the hoop with negligible interfering with its motion (see Fig. 2.21). To keep the initially bent and tied hoop stand on liquid, we use two transparent long, thin films with narrow gap as a guide which the hoop in between could lean against. The guide films are weak enough to be bent by a little interference so that we can distinct whether the jump is interfered or not from the movement of reflected light on them.

2.4 Jumping of an elastic hoop on water

2.4.2 Hydrodynamic forces of Jumping on water

There are various forces acting on the hoop pushing the water surface due to drag, buoyancy, added mass, surface tension and viscosity. Each force can be scaled as $F_d \sim \rho_f w L U^2$, $F_b \sim \rho_f g w L h$, $F_a \sim \rho_f w c L a$, and $F_s \sim \gamma L$, $F_v \sim \mu c L U / R$, respectively, where ρ_f is water density, L the effective length of hoop contact with the water surface, w the hoop width, c the thickness, g the gravitational acceleration, U descending speed of the bottom of the hoop, a descending acceleration, γ surface tension coefficient of water. We tested various range of hoop dimensions and initial deformations of hoop to observe the wide range of performance of hoop on water surface. When the initial bending energy of the hoop is too low to jump off water, the hoop vibrates near or on the water surface, whereas the hoop apparently jumps off. This study focused on the apparent jump of elastic hoops on water. In that case, the ratios between forces exerted by water imply that the apparent jump on water with descending speed of bottom of the hoop U faster than 10^{-1} is mainly propelled by drag from the liquid, showing force ratios with respect to drag scaled as $F_b/F_p \sim 10^{-2} - 10^{-1}$, $F_a/F_p \sim 10^{-2} - 10^{-1}$, $F_s/F_p \sim 10^{-1} - 10^0$, $F_v/F_p \sim 10^{-5} - 10^{-4}$. These ratios suggest that drag affects the major effect on the hoop jumping off liquid.

2.4.3 Takeoff velocity of hoops on water

Once an elastic hoop is released, it pushes down the water surface. We observed the descending bottom of the hoop moves the water surface down fast enough, the hoop takes off at the moment when the descending speed of bottom of the hoop becomes maximum value, that is, when the hoop recovers its original circular shape. By considering the hoop vibration and drag by water, the takeoff velocity of the hoop from water can be obtained as following.

The distance between center of mass and the bottom of hoop (l) is sum of the height of the center of mass of the hoop with respect to the free

2.4 Jumping of an elastic hoop on water

surface (y) and the depth of bottom of the hoop pushing the liquid (h) as shown in Fig. 2.22. Hence, the velocity of bottom of the hoop with respect to the center of mass $U_r(0, t)$ is sum of the rising velocity of center of mass of the hoop (v) and the descending velocity of the bottom of the hoop (v_d). The rising velocity of the center of mass of the hoop can be determined as $v = \int F dt/m$, with m being hoop mass, from momentum conservation. Drag would be $F \approx \int \frac{1}{2} \rho_f C_D w r (U_r(\theta, t) - v)^2 d\theta$, where ρ_f is the density of water, C_D drag coefficient, θ the angle along the hoop circumference of the contact area of the hoop with liquid. With simplified hoop vibration as sinusoidal function, we can get a sires of differential equations below.

$$Y'' = \phi(\sin T)^2 \left(\frac{5}{4} \theta + \frac{15}{16} \sin 2\theta + \frac{1}{16} \sin 4\theta + \frac{1}{48} \sin 6\theta \right), \quad (2.16)$$

$$H'' = \frac{1}{2} \cos T - Y'', \quad (2.17)$$

$$\theta'' = \frac{H'' + G_1 + G_2 + G_3}{R \sin \theta - \frac{3}{4} \cos T \cos \theta \sin 2\theta}, \quad (2.18)$$

where $Y = y/\delta$, $H = h/\delta$, $R = r/\delta$, $T = \omega t$, $\phi = C_D \rho_f \delta / 64 \pi c$, and functions G_1 , G_2 , and G_3 are as below.

$$G_1 = -R(\theta')^2 \cos \theta + \frac{1}{2} (\theta')^2 \cos T (3 \cos \theta \cos 2\theta - \frac{3}{2} \sin \theta \sin 2\theta), \quad (2.19)$$

$$G_2 = \frac{3}{4} \theta' \sin T \cos \theta \sin 2\theta, \quad (2.20)$$

$$G_3 = \frac{1}{2} \cos T (1 - \cos \theta \cos 2\theta - \frac{1}{2} \sin \theta \sin 2\theta). \quad (2.21)$$

These equations can be solved with initial conditions of $Y(0) = Y_i$, $Y'(0) = 0$, $H(0) = H_i$, $H'(0) = 0$, $\theta(0) = \theta_{c,i}$, and $\theta'(0) = 0$. Takeoff velocity of a hoop based on the velocity at the moment of shape recovery agrees well with experimental data as shown in the Fig. 2.23.

2.4.4 Efficiency of jumping on water

On a rigid solid, the takeoff velocity of jumping hoop is $\omega \delta / 2$, half of initial deformation multiplied by the natural frequency of the hoop with fixed one end, resulting the non-dimensional takeoff velocity $V = v / \omega \delta =$

2.4 Jumping of an elastic hoop on water

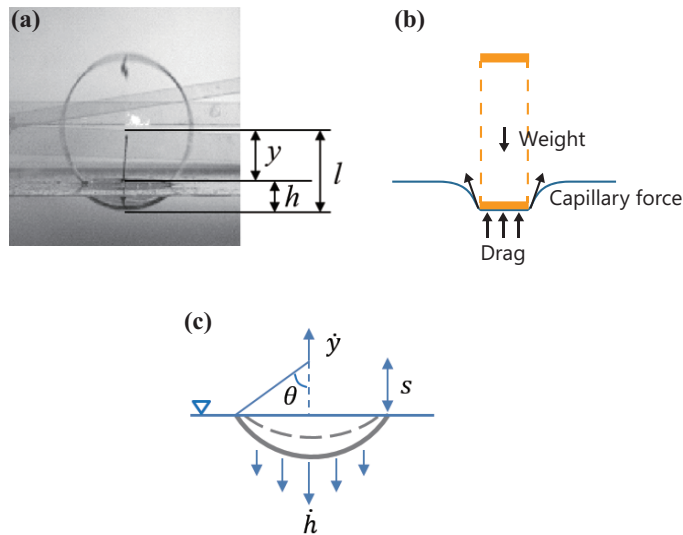


Figure 2.22: (a) Coordinates of a hoop jumping off water. (b) Forces on a hoop pushing down the water surface. (c) Coordinates of the wetted circumference element of a hoop.

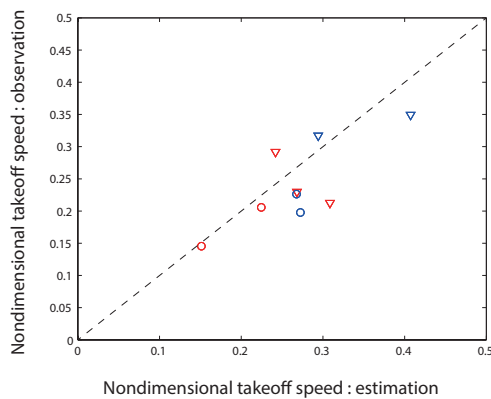


Figure 2.23: Non-dimensional takeoff velocity of hoops off water. Experimentally measured dimensionless takeoff velocity of hoops with the line indicating the theoretical expectation. Symbols: hoop thickness $75 \mu\text{m}$ (wedges), and $125 \mu\text{m}$ (circles), and hoop radius 10 mm (red), and 15 mm (blue).

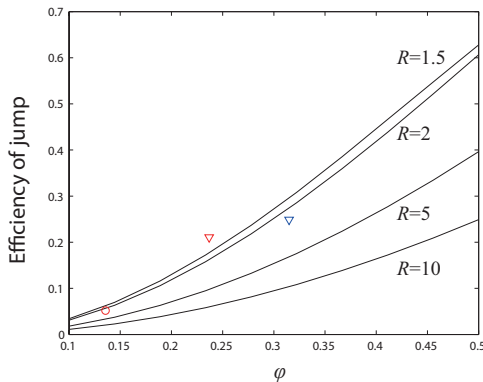


Figure 2.24: Energy transfer ratio from initial bending energy to translational kinetic energy of jumping hoops off water. The symbols are the same as those in Fig. 2.23.

0.5. In contrast, on water, the non-dimensional takeoff velocity varies with dependency on ϕ and R as shown in Fig. 2.24.

2.5 Conclusions

In this chapter, we have analyzed jumping dynamics of elastic hoops on various substrates such as rigid solids, flexible solids, and water. The elastic hoop would be the simplest mechanical system which can release initially stored elastic energy in its body leading to stable jump off the substrates including the water surface. Our study shows how the jumping performance of hoops would differ depending on the interaction between the hoop and the substrate on which the hoop launches.

If the hoop releasing its initially stored elastic energy can freely vibrate without any interference by wall, the almost all of elastic energy would be transferred to the energy related with vibration with respect to the center of mass. On the other hand, when the hoop initially contacts with a rigid solid, the specific ratio of initial energy is transferred to the translational kinetic energy, and the rest of initial energy is transferred to energy related with vibration and friction. The specific ratio of the energy transfer to

2.5 Conclusions

translational kinetic energy depends on the mass distribution of the hoop, for example 0.615 or 0.57 for our uniform hoop without or with energy loss, respectively.

When it comes to the deformable substrates, the reaction of the substrates is most important. On a flexible solid, the hoop pushing down the substrates is propelled upward by forces due to inertia and elasticity of the substrate. Therefore, the proportion of energy transfer to translational kinetic energy of the jumping hoop, or the jumping height ratio with respect to the jumping height on a rigid solid, depends on the ratio of natural frequency and ratio of stiffness of basal and jumping hoops. With the extremely small and large natural frequency ratio of the substrate to the jumper, the jumping is similar to that on the rigid solids due to the large inertia and the high stiffness of the substrate, respectively. When natural frequency of two hoops are similar, the resulting jumping height considerably varies, and we observed takeoff velocity variation from 0.4 times to 1.2 times the height on a rigid solid.

On water, the dominant force differs depending on the dimensions, stiffness, density and initial deformation of hoops. Our hoops show dimensions and mass similar to semi-aquatic insects such as water striders, but jump off water with considerably lower efficiency because of the different mechanism from water striders: water striders mainly exploit capillary force, while our hoops mainly exploit dynamic pressure like basilisk lizards.

Although we suggested an elastic hoop as one of artificial jumper showing similar performance to insects, there is a significant difference between this artificial jumper and living creatures. Because living creatures have to conduct multi-functional task, their body are not optimized to purely jump fast. Each of them carries a load, its body mass, which has concentrated mass corresponding to almost of whole mass of the insect. Whereas, the elastic hoop can be considered as the extreme cases that the concentrated mass becomes zero, remaining only a appendage required to jump. This study with the simplest system is the first step to investigating different kind of jumpers. The understanding of hoop jumping can be developed

2.5 Conclusions

to the possible jumping performance of robots carrying a heavy module at the center of the body like the insects. Furthermore, it provides the basis of further research on jumping of more complex systems. The result of this study, elucidate the artificial jumpers mimicking small jumpers in the wild, can guide both behavioral ecology to reveal the adaptation of jumping arthropods and the development of biomimetic robots maneuvering arbitrary terrains.

Chapter 3

Jumping of insects on deformable substrates

3.1 Introduction

Many insects jump to escape from predators, to move long distance, or to launch into flight. Some of them can jump on deformable substrates as fast as on rigid ones despite seemingly energy-dissipating action of such surfaces as water, leaves, or stems. The insect jumping on ground has been intensely studied (Bennet-Clark, 1975; Bennet-Clark & Lucey, 1967; Brackenbury & Hunt, 1993; Sutton & Burrows, 2011), whereas the understanding of jumping on water or leaves still remains far from complete. In this work, our major interest lies on understanding the dynamics of insect jumping on water and leaves, which will elucidate how the insects modulate their behaviors to gain fast takeoff speed on deforming substrates. We observed and modeled water striders jumping on water and grasshoppers jumping on artificial stems. By considering the joint mechanisms and appendage movement of insects, we analyzed and compared the different jumping mechanisms of these two insects and resulting performance. Then we reveal that each insects characteristic movements are properly coordinated to thrust on the substrates around its habitat. The result can provide a guideline to develop small scale biorobots traveling the wild.

3.2 Jumping of grasshoppers on artificial stems

3.2.1 Experimental Methods

Grasshoppers (*Acrida cinerea*, *Atractomorpha lata*, *Oedaleus infernalis*, and *Shirakiacris shirakii*) were collected from field of reeds near seaside and riverside around the city Incheon. Insects were placed individually on an artificial stem that is adjusted horizontal with a grasshoppers lie on it, and their jumping behaviors were recorded from the side view, using a high-speed cameras (TS 1000ME) at 500 frames per second. Jumps of adult grasshoppers were recorded and analyzed, where the jump kept in the focal plane. Most of jumps were induced by threatening with human hand or tweezers; all the analyzed jumps were checked to verify that the jumping motion was not influenced by the hand or the tweezers. The animals used in the present study were handled in accordance with institutional guideline for the care and use of laboratory animals.

The artificial stems were rectangular beam made of thick paper, with width 20 mm and thickness 0.5 mm where the length of paper beam varies 60 – 180 mm showing similar natural frequency to natural stems with low height (tens of centimeters long). In addition, a 5 mm-thick beam also used as a rigid solid like rocks.

3.2.2 General features of grasshoppers jumping on artificial stems

Figure 3.1(a) shows a typical jumping sequence of a grasshopper (male *Shirakiacris shirakii*) taken by a high-speed camera. At rest, the grasshopper holds the beam with front legs and flexes its hind legs. Once the insect initiates a jump by pushing the artificial stem with its hind legs downward and backward, the stem bends and recedes. Unlike the water surface, a stem deforms asymmetrically leading to one side (the distal tip) with larger deformation. Most grasshoppers lie on the beam with their head in the direction of the tip of beam and jump upward and forward that enables exploit thrust from both stiffness and friction on the curved beam. During

3.2 Jumping of grasshoppers on artificial stems

the impulse phase lasted 10 ms, the grasshopper gained 4 m/s of velocity of body center, with negligible velocity decrease with respect to the velocity of leg extension rate described by open circles and filled circles respectively in Figure 3.1 (d). Little difference between velocity of leg extension and body center implies the jumping performance would be as efficient as jump on the rigid surface.

Unlike water striders jumping, the contact point on the stem with tarsus of the grasshopper is kept fixed, there is only one phase of thrust, pushing. Although some cases when rebound phase occurs were observed, the grasshopper does not seem to intend to exploit bouncing stems, rather it seems to bother the insects by increasing the rotation of the body. After retouching with the leg, the body suddenly rotates showing a small decrease in velocity of body center.

3.2.3 Model of jumping locomotion of grasshoppers

Jumping grasshopper on an elastic beam can be simplified 2-DOF system consisting of the characteristic locomotion function of grasshoppers and elastic properties of the beam as shown in Figure 3.3. The beam can be modified as a simple linear spring in the vertical direction with given bending modulus and dimensions, otherwise, the locomotion function of grasshopper have to be constructed based on their thrust mechanism.

Hind leg of grasshopper extends and flexes by antagonistic motion of two muscles, extensor tibia muscle (thicker muscle in Fig. 3.2(a) illustrated by red line described in Fig. 3.2 (b)) and flexor tibia muscle (thinner muscle aligned along the extensor tibia muscle illustrated by blue line). Initially flexed hind leg by contraction of flexor muscle extends as the contraction of extensor muscle, meanwhile the moment generated by extensor muscle transferred to the force acting on the tarsus pushing the substrate. By considering the angle of extensor tibia muscle and extending hind tibia, leverage ratio between the joint and tibia, the angle of tibia with respect to the substrate, the vertical thrust of rotating hind leg of grasshopper can be obtained as $f_y = 2Frl^{-1}\sin\beta\sin\beta\cos(\theta/2)$, where f is thrust on the insect,

3.2 Jumping of grasshoppers on artificial stems

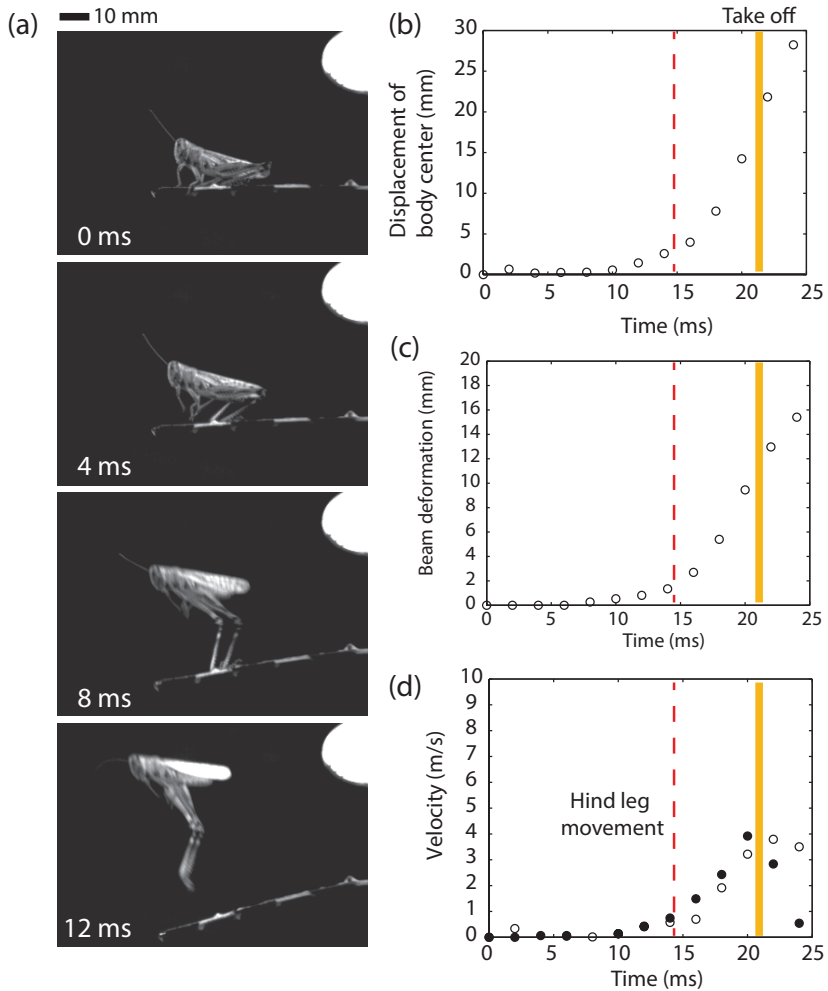


Figure 3.1: Sequence of a grasshopper (male *Shirakiacris shirakii*) jumping on an artificial stem (60 mm). (a) Captured image from record. (b) Displacement of body center in time. (c) Displacement of tip of the artificial stem in time. (d) Velocity of body center of grasshopper (open circles and leg extension rate (filled circles).

3.2 Jumping of grasshoppers on artificial stems

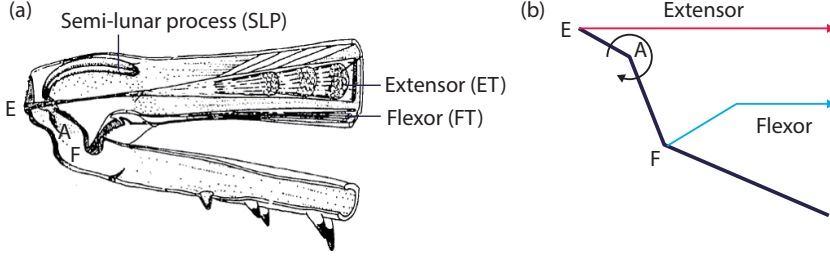


Figure 3.2: Basic mechanism of leg extension of grasshopper. (a) The femoral-tibial joint and muscle arrangement of hind leg (Bennet-Clark, 1975). (b) The schematic of thrust mechanism of hind leg. A indicates the axis of rotation, E the insertion of extensor tibia muscle, and F the insertion of flexor tibia muscle.

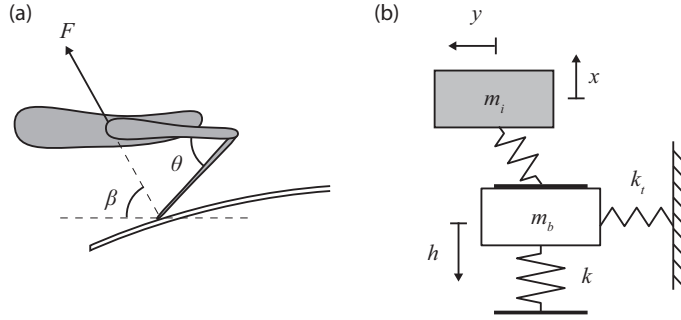


Figure 3.3: 2-DOF model of grasshopper jumping on a flexible substrate.

F tension of extensor tibia muscle, r the length between the insertion of extensor tibia muscle (E in Fig. 3.2) and the axis of rotation (A in Fig. 3.2), l the length of tibia, β the angle of line of force, and θ the angle of tibia extension. With this thrust function, a series of equations of motion of the grasshopper and the stem can be obtained in the next subsection.

3.2.4 Dynamic analysis of jumping grasshoppers on artificial stems

The equations of grasshopper jumping can be obtained as below.

$$m_i \ddot{x} = f_x, \quad (3.1)$$

3.2 Jumping of grasshoppers on artificial stems

$$m_i \ddot{y} = f_y, \quad (3.2)$$

$$m_b \ddot{h} = f_y - kh, \quad (3.3)$$

$$x \tan \beta = y + h, \quad (3.4)$$

$$x^2 + (y + h)^2 = l^2 + l_f^2 - 2l_f \cos \theta, \quad (3.5)$$

where m_i is mass of grasshopper, m_b the equivalent mass of beam, y the height of grasshopper body, h vertical deformation of beam, f_x and f_y the thrust generated by grasshoppers hind leg, k stiffness of beam, l the length of tibia, l_f the length of femur, and θ the femoral-tibia angle of leg extension. These equations are rewritten as the nondimensional form as below.

$$Y'' = 2 \frac{B}{\sqrt{1+B^2}} \sin \theta \cos \frac{\theta}{2}, \quad (3.6)$$

$$X'' = \frac{Y''}{B}, \quad (3.7)$$

$$H'' = 2 \frac{\Omega^2}{K} \frac{B}{\sqrt{1+B^2}} \sin \theta \cos \frac{\theta}{2} - \Omega^2 H, \quad (3.8)$$

$$B'' = \frac{H'' - 2X'B'}{X}, \quad (3.9)$$

$$\theta'' = \frac{XX'' + (X')^2 + (Y+H)(Y''+H'') + (Y'+H')^2 - (\theta')^2 \cos \theta}{\sin \theta}. \quad (3.10)$$

Here are five variables $Y = y/l$, $X = x/l$, $H = h/l$, $B = \tan \beta$, and θ with given parameters K or M and Ω , which are the ratio of energy generated by the insect muscle to possible maximum bending energy, or the equivalent stiffness ratio between the stem and the insect, $K = kl^2/Fr$; the mass ratio of the stem and the insect $M = m_b/m_i$; and the natural frequency ratio between the stem and the insect, $\Omega = \sqrt{(fkl^2/Fr)(m_i/m_b)}$. With the initial conditions, with initial positions and angles and initially static conditions, these equation is solved leading to the result described in Fig. 3.4-Fig. 3.7. The jumping efficiency is obtained by

$$\epsilon = \frac{0.5m_i(\dot{x}^2 + \dot{y}^2)}{Fr}. \quad (3.11)$$

3.2 Jumping of grasshoppers on artificial stems

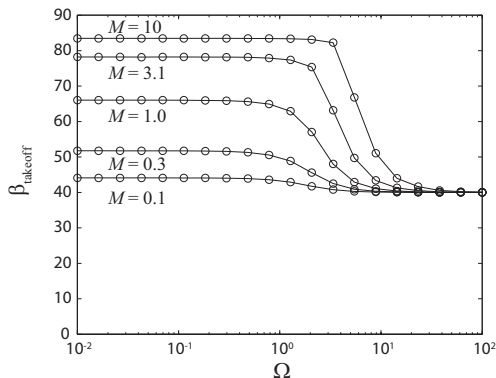


Figure 3.4: Body axis angle with respect to the horizon at the moment of take off depending on the dimensionless muscle work and mass ratio of the insect and stem.

Figure 3.5 shows the light body has advantages on jumping on flexible stems with faster take off velocity of the insect. When the natural frequency ratio is much bigger than one, the flexible stem acts as a rigid solid and is independent on the mass ratio. Dependency of initial angle of body axis and femur-tibia length ratio are also tested as described in Fig. 3.7 and Fig. 3.8.

3.2.5 Advantages of grasshoppers locomotion in jumping on stems

The results of efficiency of grasshopper jumping on flexible solids imply that higher Ω than 10 or the light body, high femur-tibia length ratio, and small angle of line of force increase the jumping efficiency. Figure 3.9 shows predicted and measured jumping efficiency of real grasshoppers. In the theory, the denominator is the muscle work Fr , however, it is almost impossible to measure the muscle tension F during the jump. Therefore, instead of Fr , resulting total energy E_{tot} at takeoff of the grasshopper and the stem is used to evaluate the jumping efficiency ($\epsilon = 0.5m_i(\dot{x}^2 + \dot{y}^2)/E_{tot}$). The total energy is sum of gravitational potential energy of the insect ($E_{i,g} = m_i g y$), translational kinetic energy of the insect ($E_{i,t} =$

3.2 Jumping of grasshoppers on artificial stems

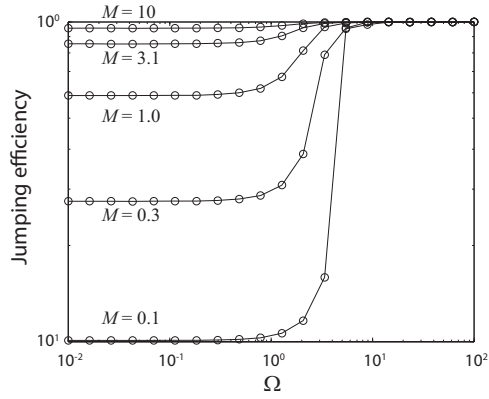


Figure 3.5: Dimensionless takeoff velocity of the insect with various muscle work and mass ratio for $L = 1$ and $\beta = 30^\circ$.

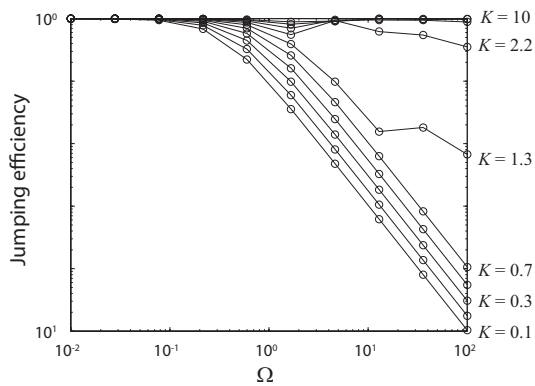


Figure 3.6: Energy transfer ratio from insects muscle work to the kinetic energy of the insect at the moment of take off.

3.2 Jumping of grasshoppers on artificial stems

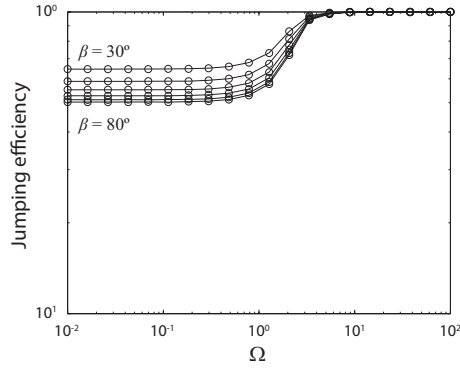


Figure 3.7: Initial angle of body axis β dependency of energy transfer ratio from insects muscle work to the kinetic energy of the insect at the moment of take off for $M = 1$ and $L = l_f/l$.

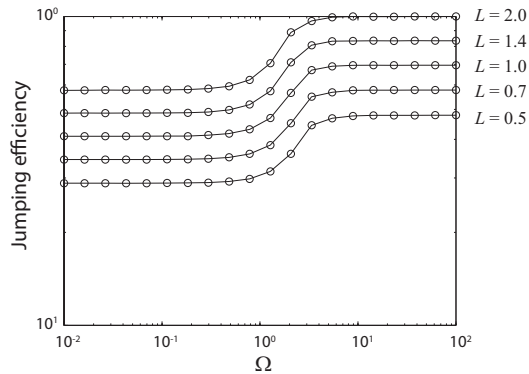


Figure 3.8: Femur length compared with tibia length $L = l_f/l$ dependency of energy transfer ratio from insects muscle work to the kinetic energy of the insect at the moment of take off for $M = 1$ and $\beta = 30^\circ$.

3.2 Jumping of grasshoppers on artificial stems

$0.5m_i(\dot{x}^2 + \dot{y}^2)$), rotational kinetic energy of the insect ($E_{i,r} = 0.5I_i\omega_i^2$), vibrational energy of the insect legs ($E_{i,v} = \sum 0.5m_{i,l}\omega_{i,l}^2\delta_{i,l}^2 + \sum 0.5I_{i,l}\omega_{i,l}^2$), gravitational potential energy of the stem ($E_{b,g} = -m_bgh$), elastic potential energy of the stem ($E_{b,e} = 0.5kh^2$), translational kinetic energy of the stem ($E_{b,t} = 0.5m_b\dot{h}^2$), and rotational kinetic energy of the insect ($E_{b,r} = 0.5I_b\omega_b^2$). Here, I_i and $I_{i,l}$ are the moment of inertia of the insect body and a leg, I_b the moment of inertia of the stem, ω_i , $\omega_{i,l}$ mean angular velocity of the insect body and the leg, and ω_b the moment of inertia of the stem. All grasshoppers show negligibly small gravitational potential energy, rotational kinetic energy of the body and vibrational energy of the legs at the moment of takeoff, resulting in almost all energy of the insect concentrated in translational kinetic energy of its center of mass.

Acrida cinerea and *Atractomorpha lata* live on grassland and jump between grasses and leaves, whereas *Oedaleus infernalis* and *Shirakiacris shirakii* inhabit gravelly fields. The species living on grass show higher jumping efficiency and lower angle of line of force. In the case of *Acrida cinerea*, it keeps the femoral-tibia joint high leading to low angle of line of force with respect to horizon. Besides, *Atractomorpha lata* has relatively longer femur than tibia (femur length is almost 1.4 times tibia length). The fixed tarsus on the stem with frictional pads and claws must have help the insect to exploit friction which acts an important role when the line of force is low resulting in an efficient jump. However, the species habitat non-deformable field show higher angle of line of force and lower jumping efficiency. The results suggest that grasshoppers living on grassland have adapted to jump efficiently on flexible surface by adjusting leg angle leading to low angle of line of force from the substrate. Further research on the behavior difference between species living on grassland and gravelly field would clarify this assumption and the jumping strategy of grasshoppers on grasses or stems.

3.2 Jumping of grasshoppers on artificial stems

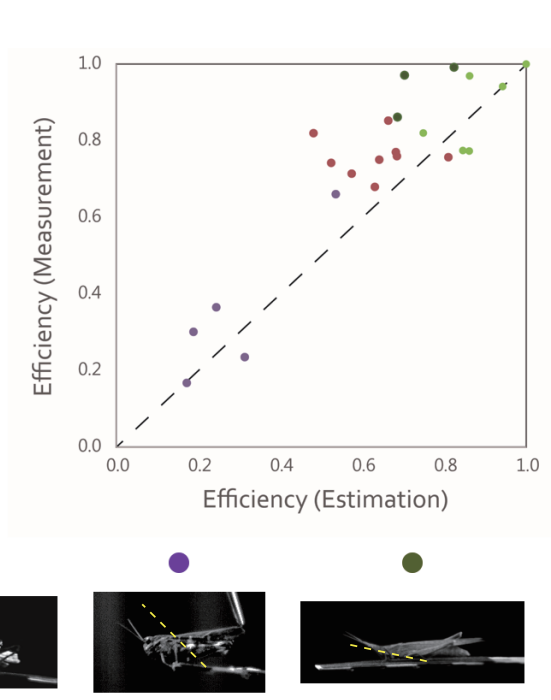


Figure 3.9: Predicted efficiency of jumping of four species of grasshoppers compared with experimentally measured data. (Yellow green) *Acrida cinerea*, (olive green) *Atractomorpha lata*, (purple) *Oedaleus infernalis*, (red) *Shirakiacris shirakii*. The yellow dashed lines on the grasshopper images indicate the line of force.

3.3 Jumping of water striders on water

3.3.1 Experimental Methods

Water striders (*Gerris latiabdominis*, *Gerris gracilicornis*, and *Aquarius paludum*) were collected from streams and ponds around the city of Seoul. Insects were placed individually in a square acrylic bath (70 mm wide) half-filled with water, and their jumping behaviors were recorded from the front and side views simultaneously, using two high-speed cameras (TS 1000ME) at 1000 frames per second. A total of 28 jumps by 21 adult water striders were recorded and analyzed, where the inclinations of jump trajectory were between 60° and 80° to the horizontal (seven jumps of four males and six jumps of three females of *Gerris latiabdominis*; six jumps of six males and two jumps of two females of *Gerris gracilicornis*; and five jumps of five males and two jumps of a female of *Aquarius paludum* with morphology described in Fig. 3.10). Most of the jumps were induced by touching the insect with a rigid stick positioned below its body; all the analyzed jumps were checked to verify that the jumping motion was not influenced by the stimulating stick.

Because we only focused on the vertical jumping speed from the water surface, we measured only the vertical component of motion of legs and bodies from the movies. The animals used in the present study were handled in accordance with institutional guideline for the care and use of laboratory animals.

3.3.2 General features of water striders jumping on water

Figure 3.11 and Fig. 3.12 shows a typical jump of a water strider taken by high-speed cameras. At rest, the water strider supports its weight using all of six legs with its body center located at y_i above the water surface. Once the insect initiates a jump by pushing the surface with the middle and hind legs downwards, dimples are made, which enable the insect to control its direction and speed of jump by transferring the momentum to the water. The dimple depth (h), measured from the unperturbed free

3.3 Jumping of water striders on water

Species	Sex	Sample size	Body mass (mg)	Length of middle leg (mm)	Length of hind leg (mm)	Wetted length of middle leg (mm)	Wetted length of hind leg (mm)	Average radius of tibia (μm)
<i>Gerris latiabdominis</i>	male	4	14.7 ± 0.3	12.5 ± 0.2	9.4 ± 0.2	7.2 ± 0.2	4.5 ± 0.1	44.6 ± 0.9
<i>Gerris latiabdominis</i>	female	3	24.6 ± 1.2	13.4 ± 0.2	10.3 ± 0.2	7.6 ± 0.1	5.0 ± 0.2	50.7 ± 4.3
<i>Gerris gracilicornis</i>	male	6	29.0 ± 2.7	18.3 ± 0.8	13.3 ± 0.6	9.9 ± 0.5	5.4 ± 0.6	65.4 ± 1.7
<i>Gerris gracilicornis</i>	female	2	48.5 ± 3.7	21.0 ± 0.6	16.5 ± 1.4	11.4 ± 0.7	7.7 ± 0.3	71.8 ± 3.9
<i>Aquarius paludum</i>	male	5	37.5 ± 1.2	24.0 ± 1.1	21.0 ± 1.3	12.7 ± 0.5	8.9 ± 0.8	65.0 ± 1.5
<i>Aquarius paludum</i>	female	1	49.0	24.4	21.4	13.2	9.1	71.0

Figure 3.10: (a) A water strider that rests and jumps on water. (b) Definition of various lengths.

surface, increases in time (t) and then decreases (Fig. 3.12(b)). The dimple depth reaches its maximum at the time t_m , which divides the stroke of the insect into two stages: the pushing ($t < t_m$) and the closing ($t > t_m$) stage. Because the average downward velocity of the four legs with respect to body center (v_d) is bell-shaped over time (Fig. 3.12 (c)), the upward velocity of the insect body (v) overtakes v_d at $t = t_m$, when the vertical growth rate of the dimple ($v_d - v$) becomes zero and its corresponding maximal depth is denoted as h_m .

In the pushing stage, the water strider drives its legs to push the water surface downwards, thereby deepening the dimple. The tarsus and tibia of each leg (Fig. 3.11) remain in contact with the water surface (Fig. 3.12(a) until $t_m = 13$ ms), and thus the total wetted length of the legs (l_w) is assumed to be almost constant and equal to the sum of length of tarsi and tibiae of four legs (l_t). In the closing stage ($t > 13$ ms), the legs continue to come close together by rotation and slide on the water surface while gradually disengaging themselves from the water surface. Due to the decreasing wetted length, over which the reaction from the water is exerted, the upward acceleration of the insect body in the closing stage is lower than in the pushing stage as seen in the decrease of body center

3.3 Jumping of water striders on water

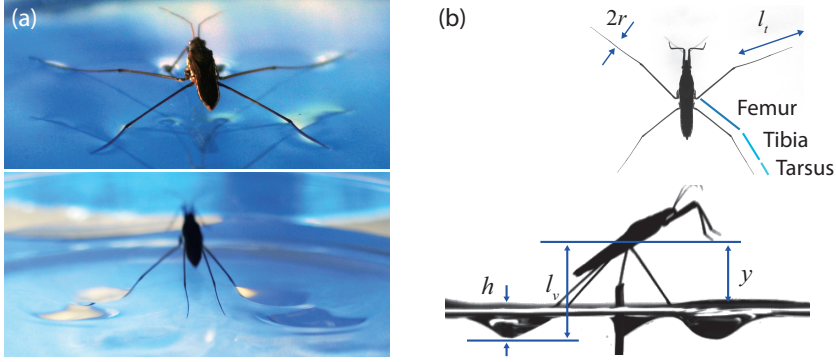


Figure 3.11: (a) A water strider that rests and jumps on water. (b) Definition of various lengths.

acceleration in Fig. 3.12(c). Upon the basis of these observations, in the following we calculate the force exerted on the strider as a function of the depth of the dimple formed by the rotating leg. The force then gives the takeoff velocity, which allows us to seek the optimal stroke condition that the strider executes to reach the maximum leaping height.

3.3.3 Hydrodynamic forces on the water striders legs

When a water strider strokes the water surface, a number of forces are exerted on the insects legs in addition to the capillary force ($F_s \sim \gamma l_w$) where γ is surface tension coefficient and l_w is wetted length of the legs, including pressure force ($F_p \sim \gamma U^2 r l_w$), buoyancy ($F_b \sim \rho g r h l_w$), inertial force due to added mass ($F_a \sim \rho r^2 l_w U^2 / h$), viscous force ($F_v \sim r l_w U / l_c$) with l_c denoting capillary length of water, and the weight of the water strider ($F_w \sim mg$). Our theoretical analysis used standard values such as density of water, $\rho = 998 \text{ kg/m}^3$; surface tension coefficient of water, $\gamma = 0.072 \text{ N/m}$; viscosity of water, $\mu = 10^{-3} \text{ Pas}$; acceleration of gravity, $g = 9.8 \text{ m/s}^2$; and average values of experimentally measured parameters for jumping *G. gracilicornis*, the medium sized water strider species: wetted length, $l_w = 30 \text{ mm}$ (evaluated from the total length of four pairs of tibia and tarsus); leg radius, $r = 50 \text{ }\mu\text{m}$ (measured at the middle of the tibia); body mass of water strider, $m = 30 \text{ mg}$; representative leg descending

3.3 Jumping of water striders on water

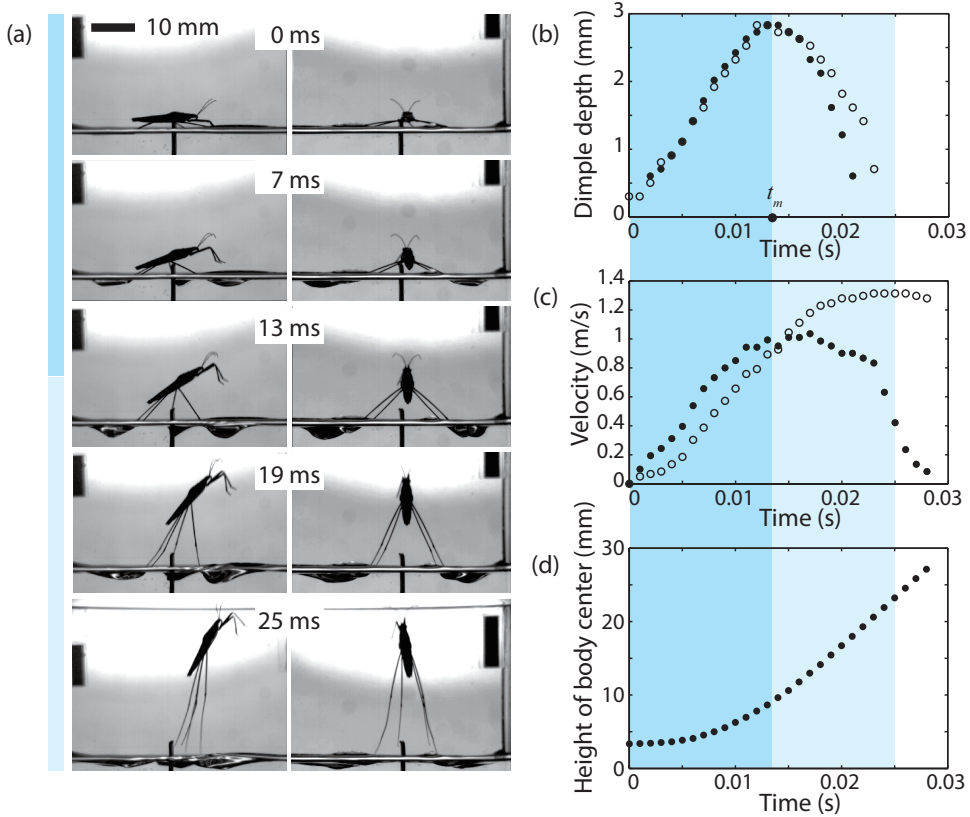


Figure 3.12: Jumping of a water strider (male *Aquarius paludum* with a body mass of 36.8 mg and an average length of middle and hind legs of 22.1 mm). (a) A representative sequence of the jump of the water strider on the water surface. (b) Average dimple depth formed by the legs (open circles for middle legs, filled circles for hind legs) during the jump. (c) Vertical velocity of the body center v (open circles) and the average downward velocity of the four legs with respect to body center v_d (filled circles). (d) Height of the body center of the water strider during the jump.

3.3 Jumping of water striders on water

speed, $U = 0.15$ m/s; and depth of dimple, $h = 3$ mm. The ratios of the other forces to the capillary force are scaled as $F_p/F_s \sim 10^{-2}$, $F_b/F_s \sim 10^{-2}$, $F_a/F_s \sim 10^{-4}$, $F_v/F_s \sim 10^{-5}$, and $F_w/F_s \sim 10^{-1}$. These ratios suggest that the capillary force dominates over the other forces, allowing us to treat the seemingly complex phenomenon of jumping on the water surface as a surface tension-dominant interaction of a long thin flexible cylinder with the water surface.

Since water strider legs bend during a jump, the flexibility of the cylinder needs to be taken into account in modeling the force exerted on the legs. Vella(Vella, 2008) provided the numerical solutions of capillary force acting on a long thin flexible cylinder clamped horizontally at one end and held at a given depth under the free surface. According to the study, the capillary force on a rigid thin cylinder can be written as

$$F_r = 2\rho g l_c l h \sqrt{1 + \left(\frac{h}{2l_c}\right)^2}, \quad (3.12)$$

where l denotes the wetted length of the cylinder, and $l_c = \sqrt{\gamma/\rho g}$ the capillary number. F_r monotonically increases with the depth of dimple h while $h < l_c$. For a flexible cylinder, the scaled length $L_f = l/l_{ec}$ plays an important role, where $l_{ec} = (Bl_c/\gamma)^{1/4}$ is the modified elasto-capillary length of the cylinder with bending rigidity $B = \pi E r^4/4$. Here E corresponds to Young's modulus of insects cuticle and r is the radius of leg. Vella presented the numerical solutions of supporting force on bent cylinders with various L_f revealing that flexibility hardly changes the shapes of the force curves with different depth, but decreases the magnitude of the force quantitatively. In other words, more flexible cylinders having larger L_f generate weaker supporting forces.

To transform the numerical solutions into more practical forms, here, we suggest an approximate force equation by introducing a flexibility factor C of the cylinder as a function of L_f . Then the capillary force on a flexible cylinder is simply estimated as

$$F = 2\rho g l_c C l h \sqrt{1 + \left(\frac{h}{2l_c}\right)^2}. \quad (3.13)$$

3.3 Jumping of water striders on water

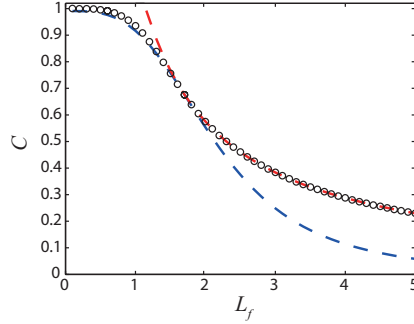


Figure 3.13: Flexibility factor. A flexibility factor C of a long thin flexible cylinder as a function of the scaled length L_f . Circles correspond to the numerically calculated values of C ; the blue dashed line $C = (1 + 0.082L_f^{3.3})^{-1}$, and the red dashed line $C = (1.15L_f)^{-1}$. The blue dashed line is used in this study for $L_f < 1.5$.

As a result, the effective wetted length becomes Cl . C was calculated by averaging the ratio of the numerical solution of the capillary force on a flexible cylinder to the asymptotic solution of that on a rigid cylinder for various L_f . Given standard liquid properties and gravitational acceleration, we simplify C into a function of L_f using the curve fit $C \approx (1 + 0.082L_f^{3.3})^{-1}$ for $L_f < 2$ or $C \approx (1.15L_f)^{-1}$ for $L_f > 2$ (Fig. 3.13). The factor C decreases with L_f , implying weaker capillary force on the more flexible cylinder. To calculate flexibility factor of water striders, we used the relationship $C \approx (1 + 0.082L_f^{3.3})^{-1}$ as indicated by blue dashed line in Fig. 3.13, since all the water striders tested have the scaled length L_f shorter than 1.5.

3.3.4 Model of locomotion of water striders jump

When water striders propel on water, they mainly use their middle legs. The middle leg is controlled by two bundles of muscle, a pair of promotor and remotor generating to-pro motion, and a pair of levator and depressor produce up-down motion as shown in Fig. 3.14. We observed that water striders rotate their middle leg backward and downward as shown in Fig. 3.15 leading to the increase of inclination angle of the insect body and

3.3 Jumping of water striders on water

closing of middle and hind legs to the middle of them with vertical stroke.

To model the vertical velocity of a water striders center of mass, the forces acting on its four legs were added. In the model, we assumed that all the legs involved in the propulsion move synchronously and leave the surface at the same time. The validity of this assumption is verified by correlation analysis between the moments of the maximum dimple depth of middle and hind legs in each trial, resulting in the correlation coefficient $r = 0.943$, p-value = 0.0311, and $df = 28$ (Fig. 3.16). Under these conditions, the force F can be expressed with C and h being the mean values of the flexibility factor and the dimple depth of the four legs, respectively, and l_w being the total wetted length of the four legs.

To solve Eq. (3.13), the wetted length (l_w) should be given. From the observation of the jumps of water striders on water, we take the wetted length to be the sum of length of tarsi and tibiae of four legs (l_t) in the pushing stage. In the closing stage, the legs rotate to increase their inclination angles from the water surface leading to apparent decrease of flexibility factor C . Furthermore, the wetted length also decreases while the legs disengage themselves from the water. To solve the differential equation of dimple growth and decay, we simplified the wetted length in the closing stage to

$$l_w = l_t(\pi - \omega t)/(\pi - \omega t_m)(H/H_m). \quad (3.14)$$

This consists of three terms: the wetted length in pushing phase l_t and the two terms that decrease with the phase of leg rotation (ωt) and dimple depth (H), corresponding to the decrease of C and l_w , respectively.

Upon the basis of our observation of the leg movement during stroke as described in Fig. 3.17, the average vertical distance between the body center and distal end of legs (l_v), and the average downward velocity of the four legs with respect to body center (v_d) are modeled as

$$l_v = l_s(1 - \frac{1}{2}\cos\omega t) + y_i, \quad (3.15)$$

$$v_d = \frac{1}{2}\omega l_s \sin\omega t, \quad (3.16)$$

3.3 Jumping of water striders on water

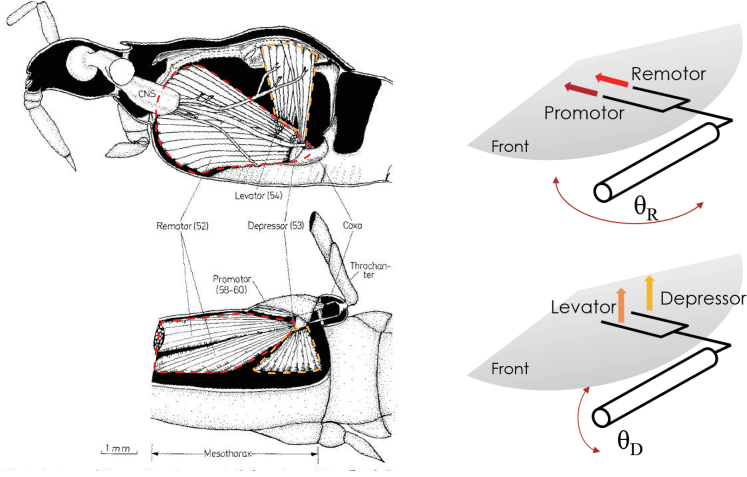


Figure 3.14: Musculoskeletal structure of middle leg of a water strider. The image of anatomical images were originally published by Demar (Murphey, 1971).

with the angular speed of the leg rotation ω and the downward stroke $l_s = l_l - y_i$, where l_l is the average length of the four legs, and y_i the initial height of the body center. The model well matches the movement of the real water strider in Fig. 3.12 as shown in Fig. 3.17. The empirical values of angular speed of the leg rotation ω , used for the nondimensional angular speed of the leg rotation $\Omega L_t^{-1/2}$, were calculated from the relationship $\omega = 2v_{d,max}/l_s$ with measured $v_{d,max}$ (maximum value of v_d) and l_s .

3.3.5 Criteria for exploiting the water surface

We observed several cases in which a leg quickly sank under the water surface after the distal end of the leg pierced the meniscus during the stroke. In these cases, the capillary force on the leg could be neglected upon penetration of meniscus because of the rapid decrease of the wetted length. This water surface piercing can be predicted from the theoretical calculations for rigid cylinders (Shi *et al.*, 2007; Vella *et al.*, 2006): the maximum displacement of the center of a thin rigid floating cylinder at the gas-liquid interface is modeled to be reached at an interfacial inclination ϕ of $\pi/2$ and

3.3 Jumping of water striders on water

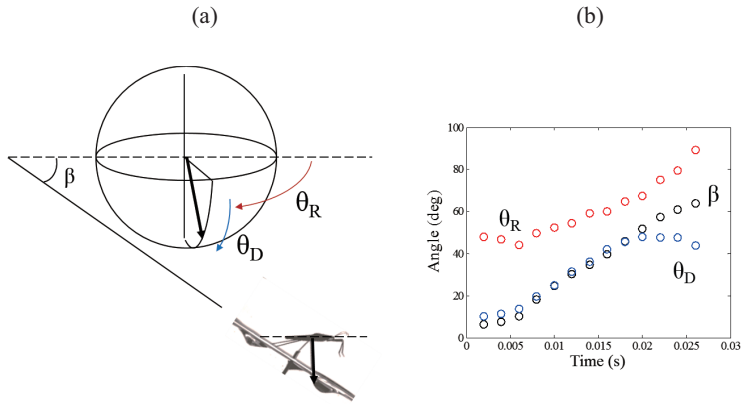


Figure 3.15: Measured angles of a water strider jumping on water.

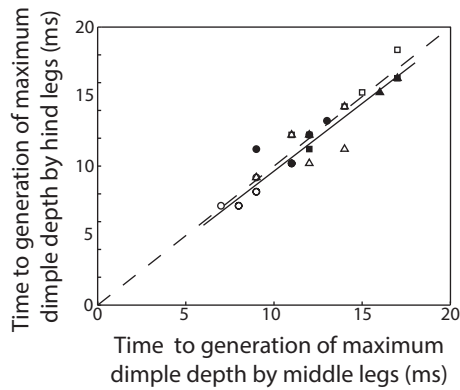


Figure 3.16: Comparison of the moment of maximum depth of dimple generation between middle and hind legs. The correlation between t_m of middle and hind legs in each trial, resulting in the correlation coefficient $r = 0.943$, p -value = 0.0311, and $df = 28$ implying the synchronous motion of four legs. Empirical results from the jump characteristics of females (filled symbols) and males (unfilled symbols) of *G. latiabdominis* (circles), *G. gracilicornis* (triangles), and *A. paludum* (squares) are also plotted. Dashed line indicates the exact match between middle and hind legs, and solid line indicates the fitted regression line.

3.3 Jumping of water striders on water

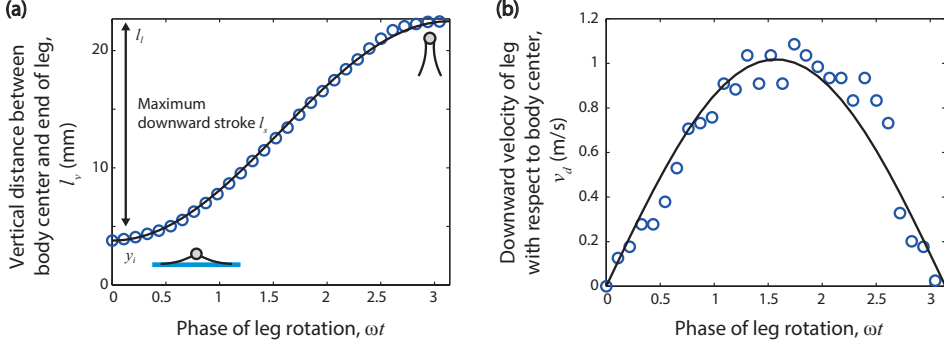


Figure 3.17: Model of leg locomotion of water strider. (a and b) Comparison of leg locomotion between the sinusoidal model and a real water strider. The solid lines correspond to the model and the circles correspond to the measurement from the movie shown in Fig. 3.12(a). (a) The average vertical distance between the body center and distal end of legs (l_v) across the leg rotation cycle. (b) The average downward velocity of four legs with respect to body center (v_d).

the displacement of cylinder (h_{max}) of l_c , as illustrated schematically in Fig. 3.18. The average depth reached by the distal end of the legs and by the lowest parts of the legs upon of the surface penetration (corresponding to the depth of dimple at the moment of penetration) were 3.72 and 4.40 mm, respectively. Both the values are comparable to the maximum theoretical depth of a floating rigid cylinder (l_c , 3.84 mm for water). Therefore, in the model, we take l_c as the critical depth h_{max} under which the surface penetration would occur.

3.3.6 Dynamic analysis of jumping water striders on water

The upward velocity of the center of mass of the insect can be determined as $v = \int F dt / m$, with m being insects body mass, from momentum conservation. Then the temporal evolution of the dimple depth $h(t)$ is given by

$$\frac{dh}{dt} = v_d \int F dt / m. \quad (3.17)$$

3.3 Jumping of water striders on water

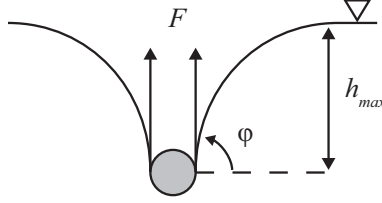


Figure 3.18: Theoretical sinking depth of a cylinder. The maximum deformation of the meniscus due to a thin rigid cylinder floating on a surface of the liquid, with the interfacial inclination ϕ and the displacement of cylinder h_{max} . The maximum displacement of the center of a thin rigid floating cylinder at the gas-liquid interface is modeled to be reached at an interfacial inclination ϕ of $\pi/2$ and the displacement of cylinder (h_{max}) of l_c .

We approximate the downward velocity of legs v_d as a sinusoidal function: $v_d = \frac{1}{2}\omega l_s \sin\omega t$ (see Fig. 3.17). Here the angular speed of the leg rotation ω and the downward stroke $l_s = l_l y_i$, where l_l is the average length of the four legs, are the parameters reflecting behavioral and morphological trait of each insect, respectively.

Combining Eqs. (3.13), and (3.17) leads to a simple differential equation of the scaled dimple depth $H(\omega t)$ as

$$H'' + 2\Omega^{-2}L_w H(1 - H^2/4)^{1/2} \frac{1}{2}L_s \cos\omega t = 0, \quad (3.18)$$

where $H = h/l_c$, $H'' = d^2H/d(\omega t)^2$, $\Omega = \omega(l_c/g)^{1/2}$, $L_w = \rho l_c^2 C l_w/m$, and $L_s = l_s/l_c$. Here, ωt is the phase of leg rotation, being 0 and π in the beginning and the end of the stroke, respectively. The dimensionless wetted length is estimated to be $L_w \sim \rho l_c^2 C l_t/m$ based on the observed visible wetted section in the pushing stage ($v_d \geq v$), while it gradually decreases due to both reduced wetted length and flexibility factor C of disengaging legs in the closing stage ($v_d < v$). Then, the temporal change of the dimple depth can be obtained by solving the differential equation with two pairs of initial conditions: $H(0) \sim 0$ corresponding to negligible initial dimple depth arising from the weight of the insect, and $H'(0) = 0$ in the beginning of the pushing stage; $H(\omega t_m) = H_m$ and $H'(\omega t_m) = 0$ at the instant of

3.3 Jumping of water striders on water

maximum dimple depth when the closing stage starts. The takeoff velocity of the water strider is defined as the velocity at the moment the dimples disappear ($H = 0$) or the legs complete their rotation ($\omega t = \pi$).

We solve Eq. (3.18) and plot the theoretically predicted maximum dimple depth and takeoff velocity as a function of the dimensionless angular speed of leg rotation $\Omega L_t^{-1/2}$ and downward stroke L_s in Fig. 3.19, which reflect behavioral and morphological trait, respectively. The maximum dimple depth increases with the greater angular speed of the leg rotation $\Omega L_t^{-1/2}$ or longer downward stroke L_s , for an individual water strider with given m , l_t , and C , and then it tends to converge to L_s . This asymptotic maximum dimple depth corresponds to the stroke with extremely high speed without any upward displacement of the body. However, the dimple depth H can grow only until the meniscus breaks (Park & Kim, 2008; Shi *et al.*, 2007; Vella *et al.*, 2006) (see Fig. 3.19).

We observed several cases in which a leg quickly sank under the water surface after the distal end of the leg pierced the meniscus during the stroke at the average depth of 3.7 mm (Fig. 3.20(c), which is close to the sinking depth of a long thin rigid cylinder $\sqrt{2}l_c$ (3.8 mm for water) (Shi *et al.*, 2007; Vella *et al.*, 2006). For a relatively long downward stroke ($L_s > \sqrt{2}$), the excessive angular speed of leg rotation $\Omega L_t^{-1/2}$ leads to penetration of water surface; this mode of jump is referred to as the meniscus breaking jump. When the meniscus does not break, the jump can be theoretically categorized into two types: pre-takeoff closing and post-takeoff closing jump, depending on whether the legs are closed before or after takeoff. In the former type of jump, the legs complete rotation before leaving the water surface ($\omega t_t = \pi$ and $H_t > 0$), whereas in the latter, the legs are fully rotated in the air after takeoff ($\omega t_t < \pi$ and $H_t = 0$). Here, t_t indicates the takeoff instant. Figure 3.20(a) demonstrates the three modes of jump, among which only two of them, post-takeoff closing and meniscus breaking, were observed for the insects used in this work.

Takeoff velocity of the insect is obtained via integrating the instantaneous force on legs, which depends on the dimple depth, over time.

3.3 Jumping of water striders on water

Figure 3.19(b) presents the predicted dimensionless takeoff speed $V_t = v_t(\rho g l_c^3 C l_t/m)^{-1}$ with different $\Omega L_t^{-1/2}$ and L_s . As the water striders stroke becomes gradually faster, or the length of tibiae and tarsi decreases, the mode of jump switches from post-takeoff closing jump to pre-takeoff closing or meniscus breaking jump depending on downward stroke L_s . For the long downward stroke ($L_s > \sqrt{2}$), the takeoff speed sharply drops as $\Omega L_t^{-1/2}$ exceeds a certain critical value because of the rupture of meniscus. Meniscus breaking jump is less beneficial because of the lack of strong support of the water surface in the late stage of jump. This may lead to not only the drag when the submerged legs rise but also destabilization of the takeoff trajectory by various disturbances, such as wind gusts or other environmental effects, to which the small animals may be more susceptible. We have verified that the theoretical prediction of takeoff speed calculated with the measured L_s and $\Omega L_t^{-1/2}$ agrees well with the experimental measurement of three species of water striders (Fig. 3.21).

3.3.7 Types of jumping and the regime map

The theoretical development so far allows us to construct a regime map for the modes of jump based on the two dimensionless parameters $\Omega L_t^{-1/2}$ and L_s in Fig. 3.22. In addition, our model predicts the optimal value of ω for the highest takeoff velocity V_t for given leg morphology. The red line, corresponding to the condition for the maximal takeoff velocity, is located in the area of pre-takeoff closing jump when downward stroke $L_s \leq 3.5$. For insects with $L_s > 3.5$, the fastest jump occurs when the insect drives its legs at the speed just below the meniscus breaking condition. Since the long downward stroke L_s can induce meniscus breaking even by a slow stroke, long legged jumpers should avoid fast stroke for efficient water jumping. We experimentally find that the jumping of water striders occurs always near the condition for the maximal takeoff velocity as shown in Fig. 3.20.

The favorable match with occasional margin for safety between the model predictions for the maximal takeoff speed and the empirical findings can be explained in biological terms as the following. The morpho-

3.3 Jumping of water striders on water

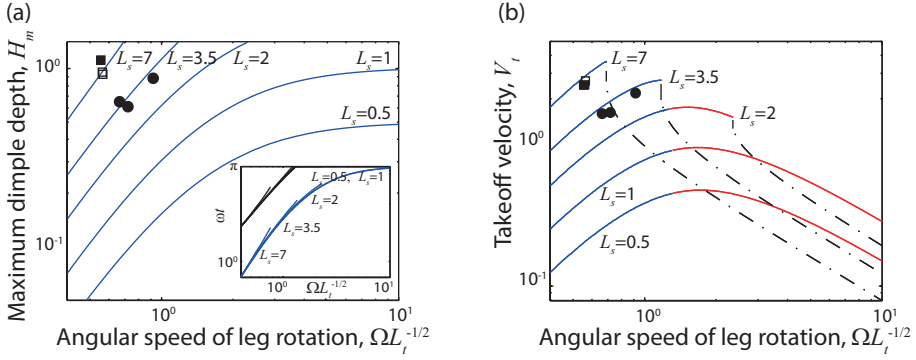


Figure 3.19: (a) Prediction of stroke. Effect of the dimensionless angular speed of leg rotation ($\Omega L_t^{-1/2}$) on the dimensionless maximum dimple depth (H_m) across a range of the dimensionless downward stroke (L_s). Inset: the phase of leg rotation at which meniscus reaches maximum depth (at $t = t_m$; blue lines), and at takeoff (at $t = t_t$; black lines). (b) Prediction of vertical jumping velocity. Prediction of vertical takeoff velocity of water striders jumping on water as a function of $\Omega L_t^{-1/2}$ for various L_s through the jump modes of post-takeoff closing (blue solid lines), pre-takeoff closing (red solid lines), and meniscus breaking (black dashed dot lines). Empirical results from the jump characteristics of females (filled symbols) and males (unfilled symbols) of *G. latiabdominis* (circles), *G. gracilicornis* (triangles), and *A. paludum* (squares) are also plotted. The empirical values of water striders with $L_s \approx 3.5$ (circles) and $L_s \approx 7$ (squares) are given.

3.3 Jumping of water striders on water

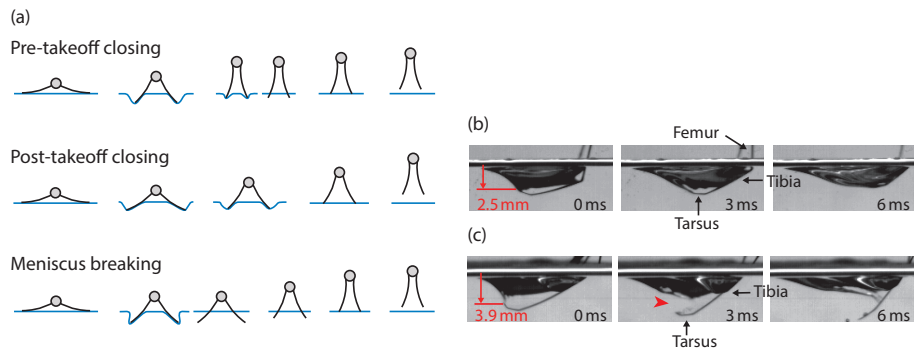


Figure 3.20: Different jump modes. (a) Schematic representation of three modes of jump: pre-takeoff closing, post-takeoff closing and meniscus breaking jump. (b and c) Magnified images of the leg and dimple in a post-takeoff closing jump ($h_m = 2.5$ mm) and a meniscus breaking jump ($h_m > 3.9$ mm): (b) the leg that does not reach the sinking depth leaves the surface unpenetrated, (c) the leg pierces the surface just below the sinking depth. The red arrow at 3 ms indicates the rupture point of the water surface. The pre-takeoff closing jump was not observed in the experiments.

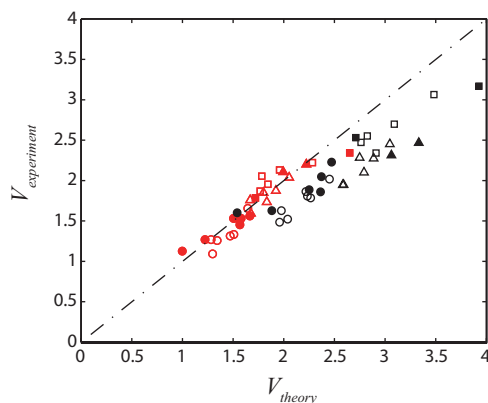


Figure 3.21: Comparison of vertical velocity. Experimentally measured, dimensionless vertical velocity of water striders versus theoretical predictions at the moment of maximum dimple depth (red symbols) and at takeoff (black symbols). Dashed dot line indicates the exact match between experiment and theory. The symbols are the same as those in Fig. 3.8.

3.3 Jumping of water striders on water

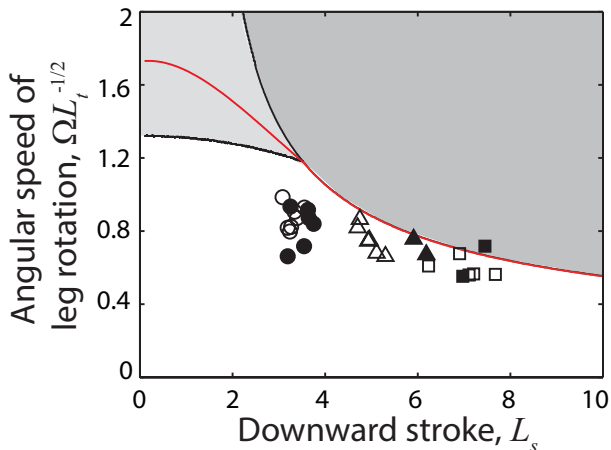


Figure 3.22: Phase diagram for the three jump modes (as a function of $\Omega L_t^{-1/2}$ and L_s): post-takeoff closing (white area), pre-takeoff closing (light shaded area), and meniscus breaking (dark shaded area). The red line marks the conditions resulting in maximal vertical takeoff velocity. Empirical results from the jump characteristics of females (filled symbols) and males (unfilled symbols) of *G. latiabdominis* (circles), *G. gracilicornis* (triangles), and *A. paludum* (squares) are also plotted.

logical traits appearing in our model, i.e. body mass, tibia plus tarsus length, whole leg length, and leg diameter, are not likely to have been optimally designed for only a single particular function, such as jump escape. However, the behavioral trait can be adjusted by individuals within the animals physical abilities. Therefore, we hypothesize that water striders control their stroke speed by modifying the rotation rate (ω) of the legs of given length to attain the maximum leaping height as a means of avoiding predation. This then leads to a question whether the optimal adjustment of the leg stroke comes from natural selection or learning through lives of individuals, which should be pursued in the future.

3.3.8 Advantages of water striders locomotion in water jumping

The high-speed imaging experiments revealed that the insect rises upward while closing its four legs inward and pushing the water surface downward (Fig. 3.12). The hydrodynamic forces generated during the leg motion include drag, surface tension, buoyancy, inertia, and viscous friction. Based on estimates of each force using representative values of parameters for the insects we observed, we found that the surface tension force dominates over the other forces for the Weber number $We = \rho U^2 D / \gamma \sim 10^{-2}$ and $Ba = mg / (\gamma P) \sim 10^{-2}$. Here, ρ is density of water, U the rate of dimple growth, D the diameter of leg, γ surface tension coefficient, m mass of the insect, g gravitational acceleration, and P the perimeter of legs. By definition, the low We due to slow stroke with thin leg implies small energy loss through water flow compared to the interfacial energy of the curved water surface. This inertia-free interaction between the legs and water surface ensures that the legs keep contacting the water surface during down stroke, thereby fully exploiting the reaction force of the curved meniscus on the legs. If the legs impacted on water with an exceedingly high speed, the water surface would retreat fast enough to lose contact with the legs and splashing would ensue, deteriorating the efficiency of momentum transfer between the legs and water surface (Shin *et al.*, 2008). The low Ba owing to light body with long perimeter indicates the capability to generate an extremely high acceleration of body compared to g by using surface tension of water. Consequently, low We and Ba collectively contribute to the high acceleration of a jumping body through surface-tension dominant interaction without notable energy loss to the water.

Since the surface tension force tends to increase with the depth of dimple, it is desirable to push the water surface as deeply as possible. However, the meniscus ruptures when the leg descends beyond a certain depth limit that the surface tension of water can endure, leading to dramatic reduction of reaction force on the jumping body (Burrows, 2013). It was already sug-

3.3 Jumping of water striders on water

gested that adaptive-deformation of joints and the flexibility of tibia and tarsus of the water striders leg may prevent the tip of leg from piercing the water meniscus and increase the supporting force of the water surface by increasing the water volume displaced (Ji *et al.*, 2012). Figure 3.23 indeed shows that the tapered leg keeps its tip pointing upward during the stroke, helping to prevent the rupture of meniscus. Utilizing a theoretical model to deduce the force acting on a flexible cylinder floating on liquid, we found that the maximum force per unit length on legs of the water striders is always near but below the value corresponding to twice the surface tension of water, 144 mN/m (Fig. 3.24). This is the maximum load that can be supported by a floating cylinder (forming two parallel contact lines).

Careful observation of the jumping sequence of the strider, Fig. 3.12, reveals that the strider rotates its middle and hind legs rather than merely pushing downward. That is, legs horizontally spread on the water surface in the beginning are stretched downwards at takeoff through rotation. To explain mechanical advantages of this leg movement, we consider what would happen if the leg morphology and kinematics were such that the strider could depress the surface only vertically without rotation. Upon reaching the maximum depth of dimple, scaled as l_c , the meniscus is recovered at a velocity of $U \sim l_c/t_r \sim 10^{-1}$ m/s, where t_r is the time scale for the capillary-gravity wave to travel the capillary length (Lee & Kim, 2008; Vella & Metcalfe, 2007). This is far lower than the takeoff velocity of the real strider, $v \sim 1$ m/s, as evidenced by the relatively slower recovery of meniscus (from 0 to 14 ms in Fig. 3.12) compared to fast disengagement of the legs from the water surface. It implies that the strider would be able to utilize the upward force from the meniscus only while the legs depress the water surface, thereby significantly reducing the momentum transfer. In reality, however, the strider rotates its legs in jumping, which ensures that the legs meet undistorted water surface continuously. Thus, the legs can keep pressing the water surface to the maximum depth during ascent of its body despite slow recovery speed of the meniscus.

3.3 Jumping of water striders on water

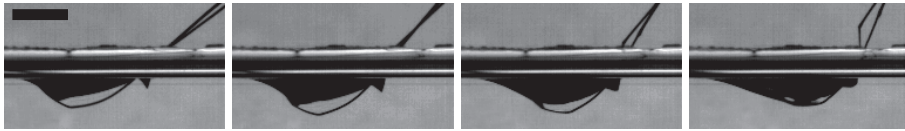


Figure 3.23: A bent leg of a water strider pushing the water surface. The tapered leg keeps its tip pointing upward during the stroke, helping to prevent the rupture of meniscus. The time gap between each snapshot is 3 ms and the scale bar indicates 5 mm.

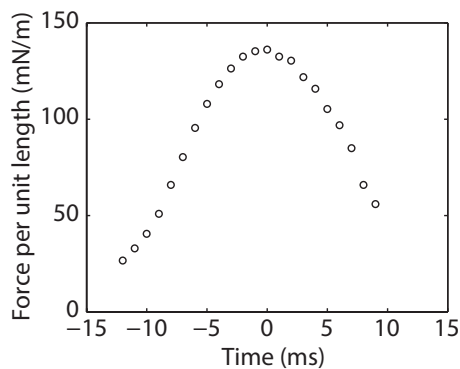


Figure 3.24: Force per unit length on the four legs of four water striders estimated from measured dimple depth and wetted length. The time is set to be zero when the maximum force is generated.

Our calculation reveals that the extended time of interaction between water surface and rotating legs of the four water striders tested leads to the increase of takeoff velocity of 27-42% as compared to the case when the legs were assumed to move only vertically. Therefore, the water striders maximize the momentum transfer to water surface by maintaining the high force profile on each leg (near 144 mN/m) until the last moment of jumping by depressing the water surface to the capillary length and rotating their legs. These strategies are applied to build an at-scale robotic water strider jumping on water elegantly (Koh *et al.*, 2015).

3.3.9 Relation between water striders morphology and water jumping

Capillary force on the legs of a water strider pushing down the water surface suggests a guide to explain the morphological trait among various species of water striders. Hu et al. (Hu *et al.*, 2003) have made a map of relation between the body mass and the maximum capillary force the striders can use among 342 species of water striders with a wide range of scale (Fig. 3.25). They suggested a critical leg length of striders to float on water, $M_c = 1$, and showed that all the striders with wide range of body mass have leg with enough long to float on water. They also gave the best fit of relation between the leg length and body mass, $F_s = 48F_g^{0.58}$, which is considerably differ from the expectation based on isometry ($F_s \sim F_g^{1/3}$). Here, we suggest one possible explanation of this unrevealed morphological trait of striders in view of jumping on water.

From the momentum conservation, takeoff velocity of the strider can be scaled as $v \sim l/t \sim Ft/m$, resulting in the time scaled as $t \sim (ml/F)^{1/2}$, and then velocity scaled as $v \sim (Fl/m)^{1/2}$, where t means the duration of pushing down the water surface and m body mass. The maximum capillary force on a leg, which is nearly proportional to the dimple depth and the wetted length, can be scaled as $F \sim hl$, where h is the maximum dimple depth and l is the representative leg length. Our model divides water jumping into two region according to the stroke length with respect to sinking depth of water. Jumpers with short stroke length, which cannot push the water surface to the sinking depth, can make dimple depth at most corresponding its stroke length. Because the capillary force on a leg is proportional to the dimple depth and the wetted length, the maximum capillary force on a driving leg shorter than sinking depth can be scaled as $F \sim l^2$. Otherwise, the jumpers with long stroke length, which can reaches the sinking depth, make dimple depth at most the sinking depth. Therefore, the maximum capillary force on a driving leg longer than sinking depth can be scaled as $F \sim l$. Because the takeoff velocity rarely differs among various

species of striders compared with the mass and length range of them, the representative leg length of the striders can be scaled as $l \sim m^{1/3}$ and $l \sim m^{1/2}$, leading to the relation between leg length and body mass as $F_s \sim F_g^{1/3}$, and as $F_s \sim F_g^{1/2}$ respectively.

These two relations match the isometry and the best fit respectively from the map of Hu et al. The most of the striders on the map having long leg length to reach sinking depth collapse on the best fit which has similar relation to our model with long stroke length, $F_s \sim F_g^{1/2}$, whereas the striders with short leg length such as the first-instar infant *Gerris remigis* described as symbol *A* in Fig. 3.25 match better with the isometry fit.

The margin between data points and the critical floating condition $M_c = 1$ means the possible acceleration of vertical jumping from water surface. Regardless of the possible power generation of living creature, the lighter striders are able to higher acceleration from capillary force. Otherwise, the heaviest strider *Gigantometra gigas* described as symbol *B* in Fig. 3.25 should use other hydrodynamic forces to vertically propel on the water surface.

3.4 Conclusions

In this chapter, we have analyzed jumping dynamics of arthropods on deformable substrates including the water surface and artificial stems. Water striders and grasshoppers are the representative jumpers on water and on land or stems, respectively, by virtue of special adaptation of their locomotion mechanisms. Our study shows how fast and how efficient their jump on deformable substrates, and provides the elucidation of the fundamentals and distinctive strategy exploited in jump.

As for grasshopper jumping, they can jump fast on land and leaves. Their jump with fixing tarsus at a specific point during the propulsion has advantages when it jumps on stems. We revealed that the locomotion speed, resulting from the ratio of the muscle tension and stiffness of the stem, mass ration between the stem and the insect, the angle of line of force, affects the

3.4 Conclusions

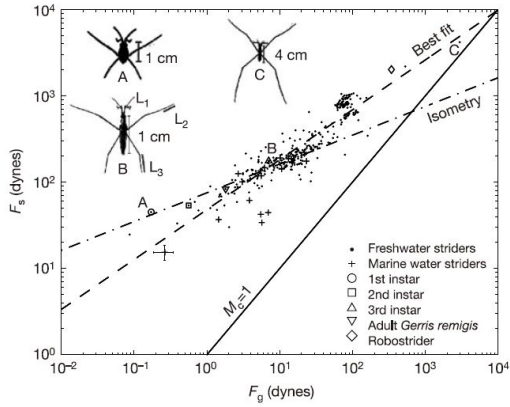


Figure 3.25: The relation between maximum capillary force $F_s = 4\gamma(L_1 + L_2 + L_3)$ and body weight of 342 species of water striders. The solid line describes the critical condition where the body weight becomes the same as maximum capillary force. The dashed dot line means the isometry condition with $F_s \sim F_g^{1/3}$. The dashed line shows the best fit to the data given by $F_s = 48F_g^{0.58}$, which has similar order to relation of the leg length and body mass based on our model. Originally published by Hu et al. (Hu *et al.*, 2003).

3.4 Conclusions

jumping efficiency. From the comparison of jumping performance between species living in grassland and gravel field, we found that grasshoppers living in vegetation perform more efficient jump on stems by keeping the angle of line of force lower showing accordance with analysis of the study.

It is known that, on the water surface, water striders can jump as fast as on land. We revealed that water striders tune their stroke speed to maximize takeoff velocity that the water surface allows. Moreover, we found that 2 DOF rotation of middle legs enables to adjust the moment profile generated in the striders muscle to fit the capillary force profile through the propulsive phase, resulting in negligible energy loss through water flow. A rational interpretation of morphological trait of wide range of scale of water striders is presented.

Our study serves as an exemplary case where a mathematical understanding is given for how a biological organism achieves the ultimate level of motility by tuning the behavioral trait. Biologists can start with our model to ask questions on the evolutionary pressure that shapes morphology and behavior of water striders, grasshoppers and other insects of similar ecology, such as springtails or small fishing spiders. Moreover, engineers can get insights required to develop multi-functional robots.

Chapter 4

An integrative view of artificial and natural small jumpers on deformable substrates

Previous sections have described the effect of deformation of substrate on small jumpers such as elastic hoops and insects. The study on the hoop jumping on the similar hoop shows broad regime with wide range of natural frequency ratio and stiffness ratio between the basal and the jumping hoop, whereas, only the vibration characteristics are concerned when it jumps on a rigid solid. The jumping locomotion regimes of artificial jumpers and insects on deformable solids can be compared each other by considering the equivalent system of water to a deformable solid.

4.1 Equivalent models of water to deformable substrates

Jumps on water of insects and hoops have analogy to jumping on basal hoop by considering capillary force and drag force, respectively. For capillary force dominant jumping, the water surface can be modified to a spring

4.2 An integrative map of efficiency of jumping on deformable substrates

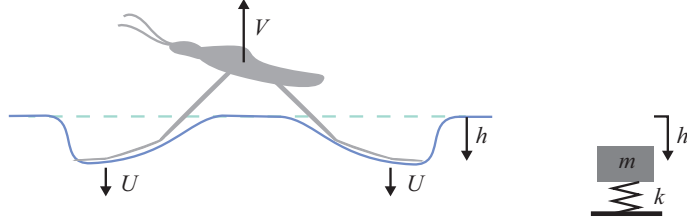


Figure 4.1: The equivalent model of water when capillary force is dominant.

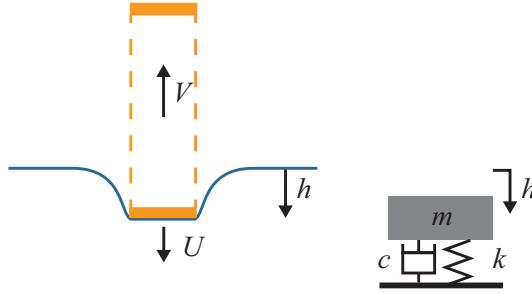


Figure 4.2: The equivalent model of water when drag force is dominant.

with stiffness $k_w \sim \rho_f g l_w l_c$, mass $m_w \sim \rho_f V$, where ρ_f is density of water, l_w is wetted length, l_c capillary length, and V volume of solid part of jumper under the free surface. The drag force can be regarded as damping effect as a function of the rate of dimple growth (\dot{h}), resulting in damping coefficient $c \sim C_D \rho_f w l_w \dot{h}^2$, and mass $m_w \sim \rho_f V$.

4.2 An integrative map of efficiency of jumping on deformable substrates

A water striders jump on water and a grasshoppers jump on a stem are shown in Fig. 4.3 (a) with the map of undamped 2DOF vibration system and the hoop jumping on water is shown in Fig. 4.3 (b) with the map of the 2DOF vibration system with damped substrates. This map shows that a water strider has extremely efficient jumping mechanism than a grasshopper on stems or a hoop on water. Water striders' exceptional performance on water exploiting capillary force shows accordance with reported jump

4.2 An integrative map of efficiency of jumping on deformable substrates

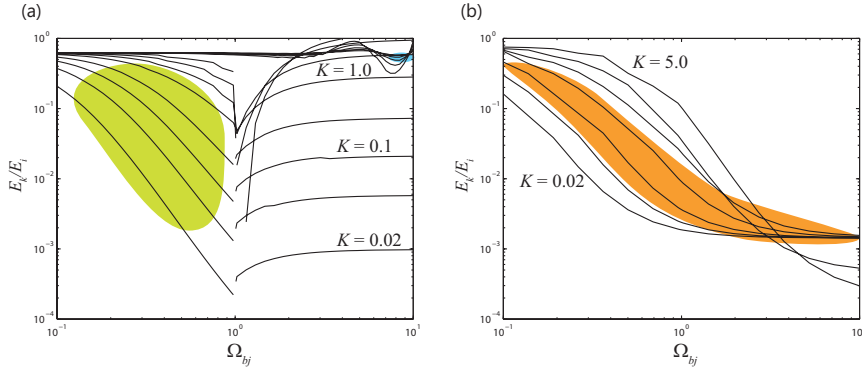


Figure 4.3: The efficiency of jump on deformable substrates of two degree of freedom system of a pair of jumper and basal hoops (a) without and (b) with damping effect. (Blue shade) water striders jumping on water, (green shade) grasshoppers jumping on artificial stem, and (orange shade) hoops on water.

on ground to the height comparable to the height on water. Although capillary force is weaker than resisting force of an elastic stem or drag force of water, when the body is ultralight, the efficiency is matchless, implying slower stroke has advantage to jump fast on water when it exploits capillary force. Damping of water reduces the difference in energy efficiency of jump, besides, it causes jumping hardly with higher natural frequency ratio than one, implying only the fast stroke can make jump itself when it uses drag force on water. For grasshoppers, they have diverse stiffness and mass ratios because of the different vegetation, therefore, they keep locomotion with lower frequency ratio than one which allows the high momentum transfer avoiding the resonance with the frequency ratio near one which can cause unstable behavior.

Chapter 5

Conclusions

In this thesis, we have presented the study on jumping of artificial jumpers and arthropods on various substrates including rigid solid, deformable solid and water, combining experimental and theoretical work. Parametric study and mathematical modeling have been performed to demonstrate the physics of jumping on various substrates.

In Chapter 2, we introduced an elastic hoop as one of simple, bio-inspired jumpers which can jump vertically, even on water, by using initially stored elastic strain energy in its body. We can control the mass, stoke and initial energy of the hoop by handling the material properties, dimensions and initial deformation of hoops so that the hoops off a wide range of jumping motion. We observed and measured the jumping of hoops on various substrates such as glass plate, basal hoops similar to the jumper, and water. And then constructed mathematical models considering the vibration characteristics of hoops and reaction force exerted by the substrates to predict the jumping performance and efficiency on various substrates.

In Chapter 3, we focused on the insect jumping on deformable substrates such as water and leaves to obtain a useful guide from behavioral and morphological traits of living creatures regulated through evolution or adaptation. Based on observation of locomotion of water striders and grasshoppers on water and stems respectively, we construct the locomotion function of each arthropod involving leg morphology and speed of stroke which are the essential parameters characterizing any locomotion. And

then, we build mathematical model to elucidate the insects jumping performance, leading to the implication of adaptation and strategy of jumping of the insects.

In Chapter 4, we compared jump of hoops and insects on all substrates we analyzed by building equivalent system of water to 2DOF spring-mass-damper systems based on the jumping mechanism on water. An integrative view of artificial and natural small jumpers on deformable substrates serves the efficiency of jumping with a given pair of a substrate and a jumper, and rationalizes how the insects make efficient jumping on flexible substrates. The result would guide to develop jumping systems on required environment.

The insects jump to avoid sudden dangers such as predators, so that jumping is a crucial mode of locomotion for survival. Although jumping has attracted intensive scientific interests, jumping on deformable substrate including water has been seldom treated from a physical point of view. Understanding how the animal achieves such a dramatic and powerful motion can shed light on the ultimate level of motility made possible through evolution. Furthermore, the investigation with artificial jumpers enables to examine various conditions leading to widened insight of the phenomena. The fundamental concepts presented in this study can also give a guideline to develop semi-aquatic robots that aim to emulate the superior maneuverability of the water strider on water and small robots traveling the wild including rocks and vegetation.

References

- BATCHELOR, G.K. (1967). *An introduction to fluid dynamics*. Cambridge university press.
- BENNET-CLARK, H.C. (1975). The energetics of the jump of the locust *schistocerca gregaria*. *Journal of Experimental Biology*, **63**, 53–83.
- BENNET-CLARK, H.C. & LUCEY, E.C.A. (1967). The jump of the flea: a study of the energetics and a model of the mechanism. *Journal of Experimental Biology*, **47**, 59–76.
- BRACKENBURY, J. & HUNT, H. (1993). Jumping in springtails: mechanism and dynamics. *Journal of Zoology*, **229**, 217–236.
- BURROWS, M. (2003). Biomechanics: froghopper insects leap to new heights. *Nature*, **424**, 509–509.
- BURROWS, M. (2006). Morphology and action of the hind leg joints controlling jumping in froghopper insects. *Journal of experimental biology*, **209**, 4622–4637.
- BURROWS, M. (2013). Jumping from the surface of water by the long-legged fly hydrophorus (diptera, dolichopodidae). *The Journal of experimental biology*, **216**, 1973–1981.
- BURROWS, M. & MORRIS, G. (2001). The kinematics and neural control of high-speed kicking movements in the locust. *Journal of Experimental Biology*, **204**, 3471–3481.

REFERENCES

- BURROWS, M. & MORRIS, O. (2003). Jumping and kicking in bush crickets. *Journal of Experimental Biology*, **206**, 1035–1049.
- BURROWS, M. & SUTTON, G.P. (2012). Pygmy mole crickets jump from water. *Current Biology*, **22**, R990–R991.
- BURROWS, M. & WOLF, H. (2002). Jumping and kicking in the false stick insect *prosarthria teretirostris*: kinematics and motor control. *Journal of Experimental Biology*, **205**, 1519–1530.
- EVANS, M.E.G. (1972). The jump of the click beetle (coleoptera, elateridae) a preliminary study. *Journal of zoology*, **167**, 319–336.
- FENG, X.Q., GAO, X., WU, Z., JIANG, L. & ZHENG, Q.S. (2007). Superior water repellency of water strider legs with hierarchical structures: experiments and analysis. *Langmuir*, **23**, 4892–4896.
- GRONENBERG, W. (1996). Fast actions in small animals: springs and click mechanisms. *Journal of Comparative Physiology A*, **178**, 727–734.
- HEITLER, W.J. (1974). The locust jump. *Journal of comparative physiology*, **89**, 93–104.
- HEITLER, W.J. (1977). The locust jump: Iii. structural specializations of the metathoracic tibiae. *The Journal of Experimental Biology*, **67**, 29–36.
- HEITLER, W.J. & BURROWS, M. (1977a). The locust jump. i. the motor programme. *The Journal of experimental biology*, **66**, 203–219.
- HEITLER, W.J. & BURROWS, M. (1977b). The locust jump. ii. neural circuits of the motor programme. *Journal of Experimental Biology*, **66**, 221–241.
- HOBBS, D.W. (1965). An assessment of a technique for determining the tensile strength of rock. *British Journal of Applied Physics*, **16**, 259.
- HOPPE, R. (1871). The bending vibration of a circular ring. *Crelle J. Math*, **73**, 158.

REFERENCES

- HU, D.L. & BUSH, J.W.M. (2010). The hydrodynamics of water-walking arthropods. *Journal of Fluid Mechanics*, **644**, 5–33.
- HU, D.L., CHAN, B. & BUSH, J.W.M. (2003). The hydrodynamics of water strider locomotion. *Nature*, **424**, 663–666.
- JI, X.Y., WANG, J.W. & FENG, X.Q. (2012). Role of flexibility in the water repellency of water strider legs: Theory and experiment. *Physical Review E*, **85**, 021607.
- KELLER, J.B. (1998). Surface tension force on a partly submerged body. *Physics of Fluids (1994-present)*, **10**, 3009–3010.
- KIRKHOPE, J. (1977). In-plane vibration of a thick circular ring. *Journal of Sound and Vibration*, **50**, 219–227.
- KOH, J.S., YANG, E., JUNG, G.P., JUNG, S.P., SON, J.H., LEE, S.I., JABLONSKI, P.G., WOOD, R.J., KIM, H.Y. & CHO, K.J. (2015). Jumping on water: Surface tension dominated jumpng of water striders and robotic insects. *Science*, **in printing**.
- LEE, D.G. & KIM, H.Y. (2008). Impact of a superhydrophobic sphere onto water. *Langmuir*, **24**, 142–145.
- LEE, D.G. & KIM, H.Y. (2009). The role of superhydrophobicity in the adhesion of a floating cylinder. *Journal of Fluid Mechanics*, **624**, 23–32.
- LOVE, A.E.H. (2013). *A treatise on the mathematical theory of elasticity*, vol. 1. Cambridge University Press.
- MURPHEY, R.K. (1971). Motor control of orientation to prey by the water-strider, gerris remigis. *Journal of Comparative Physiology A: Neuroethology, Sensory, Neural, and Behavioral Physiology*, **72**, 150–167.
- PARK, K.J. & KIM, H.Y. (2008). Bending of floating flexible legs. *Journal of Fluid Mechanics*, **610**, 381–390.

REFERENCES

- RAUX, P.S., REIS, P.M. & BUSH, J.W.M. (2010). Rolling ribbons. *Physical review letters*, **105**, 044301.
- RIBAK, G., REINGOLD, S. & WEIHS, D. (2012). The effect of natural substrates on jump height in click-beetles. *Functional Ecology*, **26**, 493–499.
- ROTHSCHILD, M., SCHLEIN, J., PARKER, K., NEVILLE, C. & STERNBERG, S. (1975). Execution of the jump and activity. *Philosophical Transactions of the Royal Society B: Biological Sciences*, **271**, 499–515.
- SHEWRY, P.R., TATHAM, A.S. & BAILEY, A. (2003). *Elastomeric proteins: structures, biomechanical properties, and biological roles*. Cambridge University Press.
- SHI, F., NIU, J., LIU, J., LIU, F., WANG, Z., FENG, X.Q. & ZHANG, X. (2007). Towards understanding why a superhydrophobic coating is needed by water striders. *Advanced Materials*, **19**, 2257–2261.
- SHIN, B., KIM, H.Y. & CHO, K.J. (2008). Towards a biologically inspired small-scale water jumping robot. In *Biomedical Robotics and Biomechanics, 2008. BioRob 2008. 2nd IEEE RAS & EMBS International Conference on*, 127–131, IEEE.
- SUGIYAMA, Y. & HIRAI, S. (2006). Crawling and jumping by a deformable robot. *The International journal of robotics research*, **25**, 603–620.
- SUTTON, G.P. & BURROWS, M. (2011). Biomechanics of jumping in the flea. *The Journal of experimental biology*, **214**, 836–847.
- VELLA, D. (2008). Floating objects with finite resistance to bending. *Langmuir*, **24**, 8701–8706.
- VELLA, D. & METCALFE, P.D. (2007). Surface tension dominated impact. *Physics of Fluids (1994-present)*, **19**, 072108.
- VELLA, D., LEE, D.G. & KIM, H.Y. (2006). The load supported by small floating objects. *Langmuir*, **22**, 5979–5981.

국 문 초 록

곤충과 탄성 고리의 도약 : 소형 개체의 수면 및 탄성체 위 도약에 대한 생체모사 역학 연구

서울대학교 대학원

기계항공공학부

양은진

도약은 작은 동물에게 매우 효과적인 운동 수단으로써, 천적으로부터의 도망, 먹이 사냥, 장거리 이동 시에 매우 중요하게 활용된다. 거품벌레, 벼룩, 메뚜기와 같이 작은 절지동물은 몸길이의 수 십 수 백 배에 이르는 높이까지 뛰어오른다. 소금쟁이와 거미와 같은 수생 절지동물은 수면에서도 높이 뛰어오르곤 한다. 이렇게 탁월한 절지동물의 도약능력에서 영감을 받아, 생체의 기본 구조와 기능, 설계를 모사한 방식의 로봇 개발 연구가 부상하고 있다. 본 연구에서는, 이론적 해석과 실험의 융합적 연구를 통하여, 단단한 고체면, 유연한 고체면, 수면의 다양한 표면에서 이루어지는, 단순한 도약 기구와 곤충의 도약의 핵심 원리를 이해하고, 도약이 이루어지는 기저의 특성에 따라서 효과적인 도약 성능을 내는 도약기구의 조건을 도출하였다.

먼저, 단순한 도약기구로서 탄성 고리의 도약 특성을

고찰하였다. 탄성 고리는 자체 내의 변형에 의한 탄성 에너지를 이용하여 도약할 수 있는, 매우 단순한 기계시스템으로서, 재료와 크기를 조정함으로써 다양한 초기 조건을 구현할 수 있다. 탄성 고리에 저장되어있던 탄성 에너지는 도약 직전까지의 추진 과정에서 탄성 고리의 운동 에너지, 진동에너지, 기저면과의 상호작용에 의한 에너지 손실 등 다양한 갈래로 전환된다. 이 에너지 전환 비율은 기저면의 반응 민감성에 따라 달라진다. 본 연구에서는 다양한 기저면에서의 탄성 고리의 운동을 단순화하여, 직관적이며 가공이 용이한 형태의 해를 도출함으로써, 유사한 시스템은 물론 복잡한 시스템에도 응용하기 적합한 도약 원리를 제공하였다.

이어서 실제 소금쟁이와 메뚜기의 수면 및 유연한 고체면에서의 도약 특성을 고찰하였다. 이 두 종은 각기 수면과 초목에서 두드러진 도약 특성을 자랑한다. 소금쟁이의 경우, 표면장력 힘을 이용하여 수면에서 매우 효율적으로 도약하며, 메뚜기의 경우, 줄기나 잎의 관성력과 탄성력을 이용하여 도약한다. 본 연구에서는 곤충의 도약 특성 관찰 결과를 바탕으로 각 곤충의 운동 특성 변수를 선정하고 운동 특성 함수를 마련하였다. 각 곤충의 운동 특성 함수와 기저면의 상호작용을 바탕으로 운동방정식으로 세우고, 곤충의 운동 특성 변수에 따른 도약 결과를 설명하는 운동 특성 지도를 작성하였다. 본 연구를 통하여 대상 곤충이 각기 서식지에 적응하여, 해당 기저면을 효과적으로 이용하는 방식의 거동을 보임을 밝혔다.

생물은 최적화된 하나의 가능한 해를 제공한다. 이 해를

하나의 기준으로 삼고, 역학적 해석 및 조작성 용이한 기계 시스템을 이용한 실험적 연구의 결합을 통하여 생물이 제시하는 하나의 해의 위상을 평가하고, 때에 따라 추가적인 최적해를 도출할 수 있다. 본 연구에서는 기계시스템과 생물에 대한 해석적 실험적 복합연구를 통하여 공학과 생물학계의 공통된 화두인 유연한 기저에서의 도약에 대한 종합적인 결과를 도출하였다. 본 연구에서 제시하는 유연한 기저에서의 소형 개체의 도약에 관한 통합적 관점은 차세대 다기능 소형 로봇의 개발에 주요한 지침을 제공하고, 운동학적 상황이 생물의 운동 행동 및 형태에 미치는 영향의 탐구를 진작시킬 것으로 기대한다.

주요어: 도약, 수면, 유연한 고체면, 소금쟁이, 메뚜기, 최적 행동, 도약 전략

학 번: 2008-20759